P-wave anisotropic tomography of the central and southern Philippines

doi: 10.1016/j.pepi.2018.12.001

P-wave anisotropic tomography of the central and southern Philippines

Jianke Fan[a, b], Dapeng Zhao[b]

[a] *CAS Key Laboratory of Marine Geology and Environment, Institute of Oceanology, Chinese Academy of Sciences, Qingdao 266071, China. E-mail: fanjianke@qdio.ac.cn*

[b] *Department of Geophysics, Graduate School of Science, Tohoku University, Sendai 980-8578, Japan*

ABSTRACT

The first P-wave anisotropic tomography of the crust and upper mantle beneath the central and southern Philippines is obtained by inverting a large number of P-wave arrival-time data of local earthquakes and teleseismic events, which sheds new light on the geodynamic evolution of the study region. Our results show that fast-velocity directions of azimuthal anisotropy in the upper mantle below 250 km depth and the mantle transition zone change gradually from NE-SW to NW-SE northwards, possibly indicating a horizontal mantle flow in and around the mantle transition zone. The existence of the horizontal flow suggests that basalts of the Indian-type mantle in the eastern part of the South China Sea possibly originated from the mantle beneath the Celebes and Molucca seas. Our results also reveal a positive radial anisotropy ($V_{pv} < V_{ph}$) reflecting a horizontal mantle flow between the Manila Trench and the northern part of the Philippine Trench, which may facilitate the subduction initiation along the northern Philippine Trench.

Key words: Seismic anisotropy; Philippine Trench; South China Sea; Mantle flow.

1. Introduction

In and around the Philippines, the Eurasian plate, the Australian plate and the Philippine Sea (PHS) plate are interacting with each other (Fig. 1). The Philippines is composed of the aseismic Palawan microcontinental block and the seismically active Philippine Mobile Belt, which has experienced various events of collision, subduction and accretion (Yumul et al., 2003, 2008).

These different tectonic events render the Philippines a unique region to better understand the interactions and geodynamic processes between the lithospheric plates.

Seismic anisotropy, a phenomenon that seismic wave velocity changes with direction, could provide important constraints on geodynamic processes in the crust and mantle, both past and present (e.g., Long, 2013; Zhao et al., 2016). Seismic anisotropy is mainly caused by shape-preferred orientation (SPO) due to large-scale aligned features such as fractures and faults in the crust, and lattice-preferred orientation (LPO) ascribed to crystal alignment and mantle flow (Zhao et al., 2016 and many related references therein). Because of the scarcity of seismic anisotropy observations in the present study region, the geologic setting and tectonic evolution of the Philippines are still not very clear.

Seismic anisotropy can be investigated using several techniques, such as shear-wave splitting, surface-wave dispersion, receiver functions, and Pn-wave tomography, etc. (see reviews by Fouch and Rondenay, 2006; Long, 2013). However, all these techniques have some drawbacks, which limit their applications. For example, the popular shear-wave splitting measurement has a good horizontal resolution, but its depth resolution is very poor. The drawbacks of these techniques can be overcome by P-wave anisotropic tomography, which can determine three-dimensional (3-D) distribution of both isotropic P-wave velocity (Vp) and Vp anisotropy in the crust and upper mantle beneath a seismic network (Zhao et al., 2016), providing important information on the 3-D structure and dynamics under a study region. In this work, we determine the first 3-D Vp anisotropic tomography of the crust and upper mantle beneath the central and southern Philippines by inverting a large number of P-wave travel-time data of local earthquakes and teleseismic events. Our results shed new light on the tectonic evolution and subduction dynamics of the Philippine region.

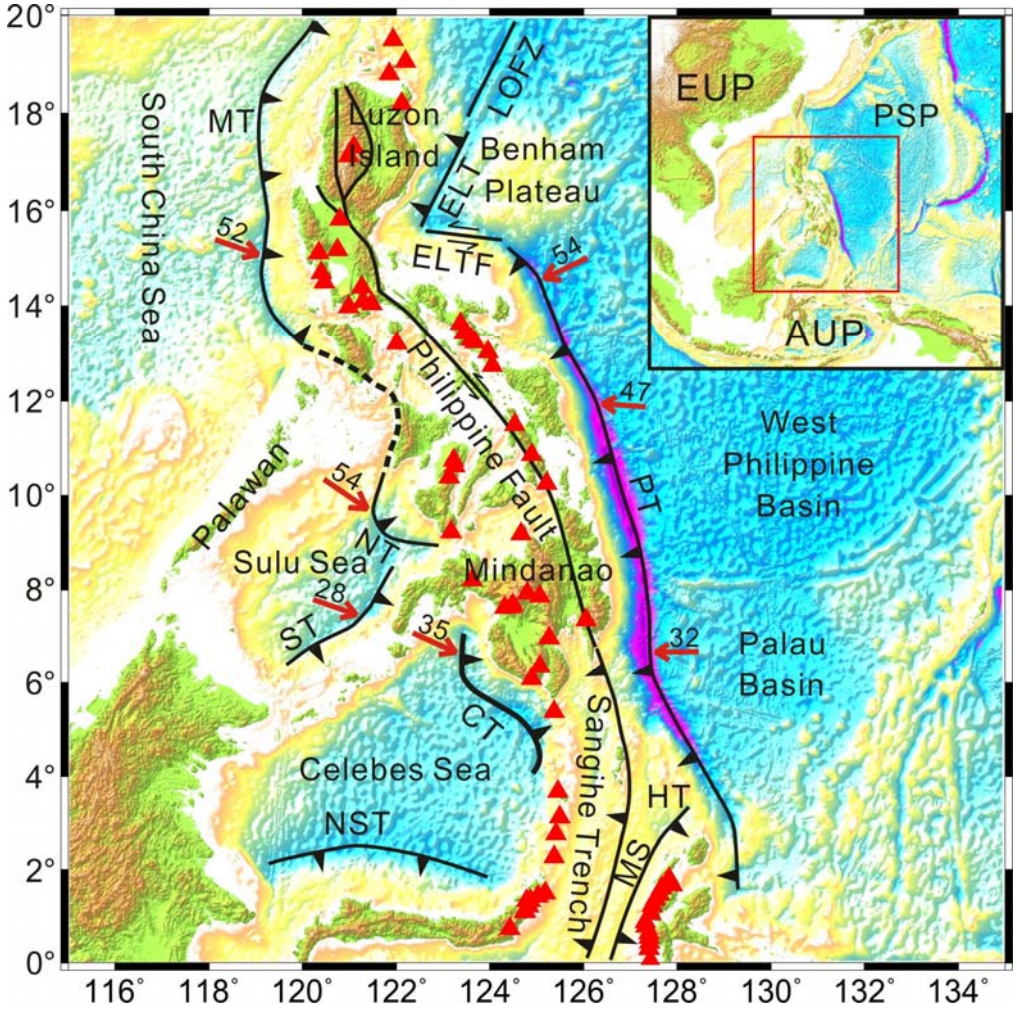

Fig. 1. Tectonic setting in and around the Philippines. The bathymetric data are from Smith and Sandwell (1997). The solid lines denote active faults, whereas the sawtooth lines denote trench axes. The black dashed line denotes a collision zone. The red arrows and the adjacent numbers indicate the convergence rates (mm/year) along the trenches (Rangin et al., 1999). The red triangles denote active volcanoes compiled by the Smithsonian Institution's Global Volcanism Program (2013). The red box in the inset map shows the location of the present study area. AUP, the Australian plate; CT, the Cotabato Trench; ELT, the East Luzon Trough; ELTF, the East Luzon Transform Fault; EUP, the Eurasian plate; HT, the Halmahera Trench; LOFZ, the Luzon-Okinawa Fracture Zone; MS, the Molucca Sea; MT, the Manila Trench; NST, the North Sulawesi Trench; NT, the Negros Trench; PSP, the Philippine Sea plate; PT, the Philippine Trench; ST, the Sulu Trench.

2. Data

Our data set includes P-wave arrival times of local earthquakes and teleseismic events recorded at 89 seismic stations in the study region (Fig. 2a), which are collected from the International Seismological Center (ISC)-EHB Bulletins from 1960 to 2013 (http://www.isc.ac.uk/isc-ehb/) (Engdahl et al., 1998; Engdahl, 2006). The local earthquakes are selected based on the following criteria: 1) each event was recorded at over four seismic stations; 2) raw travel-time residuals of each event are in a range of ±5.0 s; and 3) the study region is divided into cubic blocks with a size of 0.1°×0.1°×10 km, and in each block only one event is selected that was recorded at the maximum number of seismic stations.

The teleseismic events are selected according to the following criteria: 1) events with an epicentral distance of 30° to 90° are selected to reduce the effects of complex structures near the core-mantle boundary and the upper mantle outside the study volume (Zhao et al., 1994, 2013); 2) each event was recorded at over 4 seismic stations that are located in the present study region; 3) relative travel-time residuals of each teleseismic event are in a range of ±5.0 s; and 4) the global crust and upper mantle are divided into cubic blocks with a size of 0.1°×0.1°×10 km, and in each block only one event is selected that was recorded at the maximum number of seismic stations in the present study region (Fig. 2a).

Histograms of the P-wave travel-time residuals of the selected local and teleseismic events, show that most of the residuals fall in a range of ±2.0 s (Fig. S1). Therefore, ±2.0 s are taken as the cutoff residuals of the travel-time data used in the tomographic inversions. As a result, our final data set includes 29,801 P-wave arrival times of 3371 local earthquakes (Fig. 2b) and 21,931 P-wave relative travel-time residuals of 2938 teleseismic events (Fig. 2c).

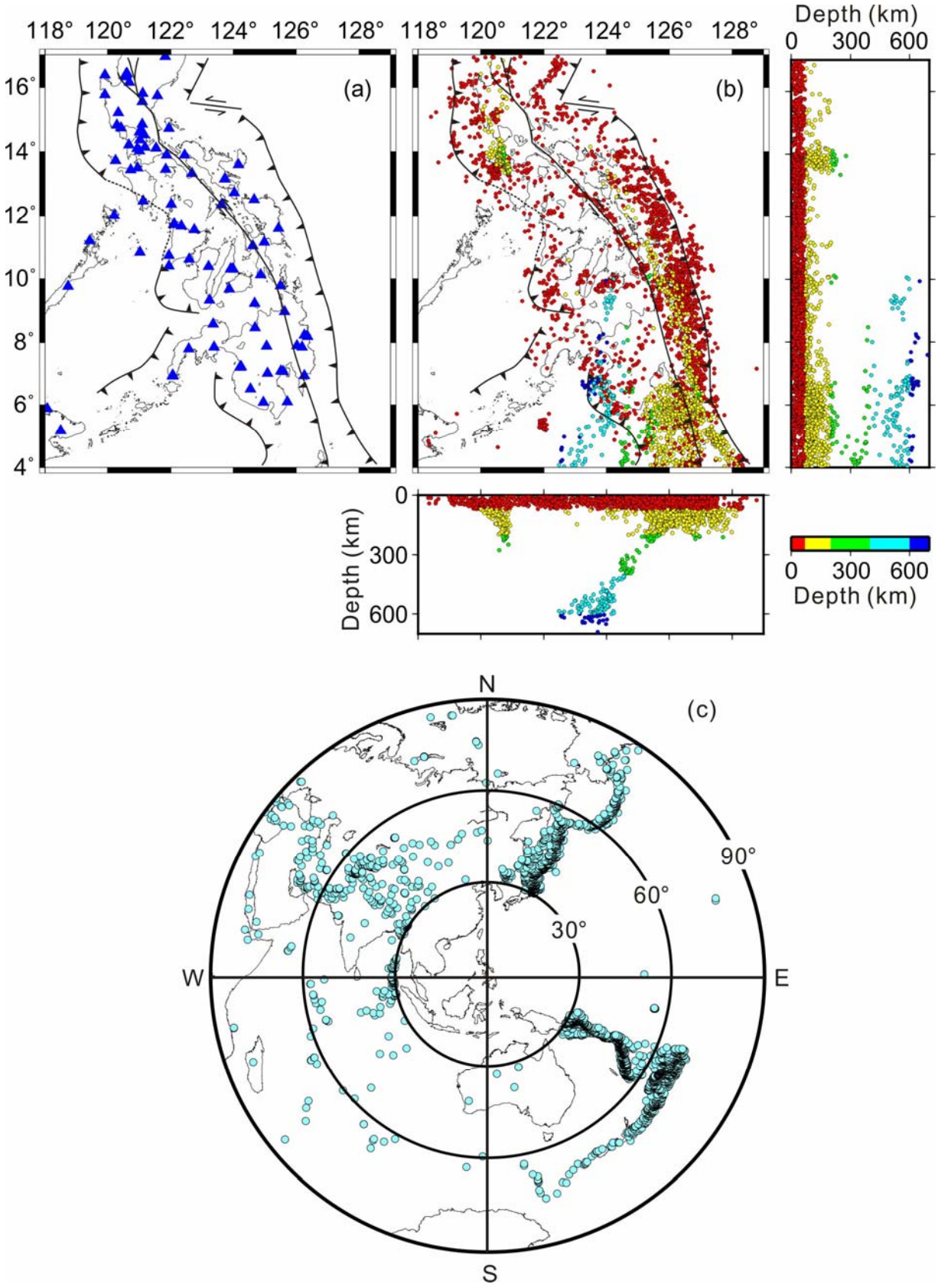
118° 120° 122° 124° 126° 128°
16°
14°
12°
10°
8°
6°
4°
(a)
(b)
Depth (km)
0 300 600
Depth (km)
0
300
600
0 300 600
Depth (km)
N
S
W
E
(c)
90°
60°
30°

Fig. 2. Distribution of (a) seismic stations (dark blue triangles), (b) local earthquakes (color dots), and (c) teleseismic events (light blue dots), which are used for tomographic inversions in this study. The colors in (b) denote the focal depths. The other symbols are the same as those in Fig. 1.

3. P-wave isotropic tomography

The isotropic tomography method of Zhao et al. (1994, 2012) is adopted to determine a 3-D Vp model of the crust and upper mantle beneath the study region. The starting 1-D velocity model is similar to that of the previous tomographic inversions in the study region (e.g., Fan et al., 2015, 2017), which is derived from the CRUST1.0 model (Laske et al., 2013), the WPSP01P model (Wright and Kuo, 2007), and the iasp91 Earth model (Kennett and Engdahl, 1991). A 3-D grid is arranged in the study volume with lateral and vertical grid intervals of 0.5° and 15-100 km (at depths of 5, 20, 50, 100, 150, 200, 250, 300, 400, 500, 600 and 700 km), respectively. Vp perturbations at the grid nodes are taken to be unknown parameters, which are solved by inverting the local and teleseismic data using the LSQR algorithm (Paige and Saunders, 1982) with damping and smoothing regularizations (Zhao et al., 1994, 2012). The optimal values of the damping and smoothing parameters are found to be 50 and 1000, respectively (Fig. S2), after conducting a series of tomographic inversions and considering the balance between the reduction of the root-mean-square (RMS) travel-time residual and norms of the obtained 3-D Vp models (Eberhart-Phillips, 1986; Zhao, 2015). After the joint inversion of local-earthquake arrival times and teleseismic relative travel-time residuals with the optimal damping and smoothing parameters, the RMS travel-time residual is reduced from 0.968 s for the initial 1-D model to 0.857 s for the final 3-D Vp model.

Our isotropic tomographic results (Figs. 3 and 4) reveal clear morphologies of the high-velocity (high-V) subducted slabs and low-velocity (low-V) anomalies beneath the active volcanoes and the collision zone between the Palawan block and the Philippine Mobile Belt at depths of 100-250 km, which are consistent with the previous tomographic results of the study region (e.g., Fan et al., 2017). The subducted South China Sea (SCS) slab is visible down to ~450 km depth with a near-vertical dip angle, which looks overturned above the mantle transition zone (MTZ) in the vertical cross-section A (Fig. 3a). The detached SCS slab is also well imaged (Fig. 3b and 3c). The high-V PHS slab is only visible at depths of 100-150 km in the cross-sections A-D (Fig. 3a-3d), significantly different from that in the cross-sections E and F

(Fig. 3e and 3f), where the subducted PHS slab could be traced down to depths of 400-500 km with an overturned dip angle. At the northern end of the Negros Trench, the Sulu Sea slab is visible down to ~200 km depth firstly with a near-horizontal dip angle and then abruptly with a steep dip angle (Fig. 3d), which is similar to that at the southern end of the Negros Trench except for a maximum depth of ~300 km (Fig. 3e). The Molucca Sea (MS) slab has subducted down to ~650 km depth along the Sangihe Trench (Fig. 3g). The low-V anomalies above the subducted SCS and Sulu Sea slabs could be traced down to ~200 km depth (Fig. 3a and 3d), indicating that arc magmatism and volcanism in the subduction zones are caused by joint effects of fluids from slab dehydration and corner flow in the mantle wedge (Zhao et al., 1994; Zhao, 2015). Low-V anomalies are visible under several active volcanoes in the Mindanao Island that may not be associated with the plate subduction (Fig. 3f), suggesting that those volcanism and magmatism may be generated by the collision between the western and eastern Mindanao since ~5 Ma (Pubellier et al., 1991; Castillo et al., 1999). The Malindig volcano near the Mindoro Island (Fig. 3b) may have the same origin.

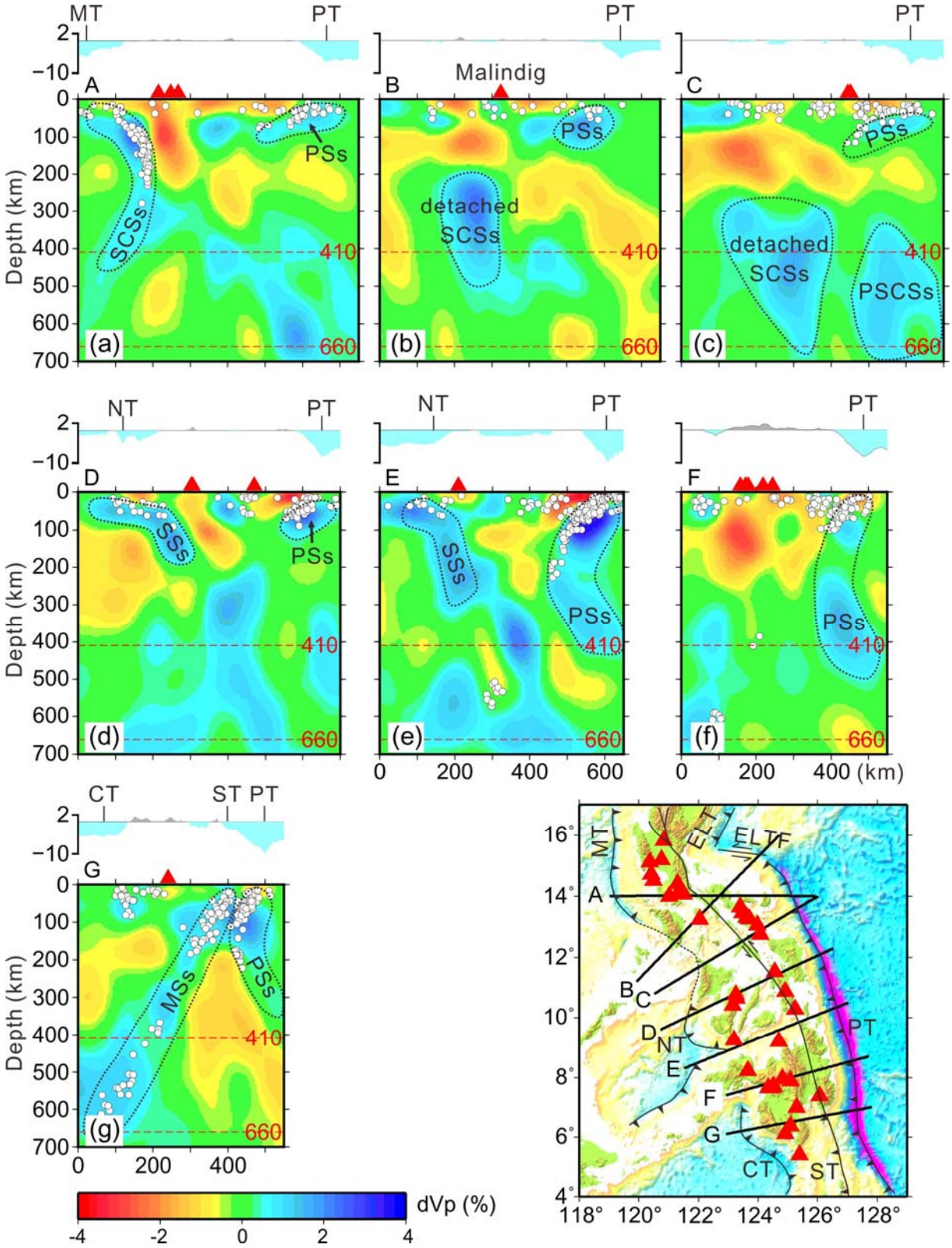
MT
PT
NT
CT
ST
Malindig
A
B
C
D
E
F
G
(a)
(b)
(c)
(d)
(e)
(f)
(g)
PSs
SCSs
detached SCSs
PSCSs
SSs
MSs
PSS
410
660
Depth (km)
0
100
200
300
400
500
600
700
2
−10
0
200
400
600
(km)
dVp (%)
-4
-2
0
2
4
ELT
ELTF
16°
14°
12°
10°
8°
6°
4°
118°
120°
122°
124°
126°
128°

Fig. 3. Vertical cross-sections of isotropic Vp tomography along seven profiles shown on the inset map. The red and blue colors denote low and high Vp perturbations, respectively, whose scale is shown at the bottom-left. The white dots and red triangles show local earthquakes and active volcanoes, respectively, within a 30-km width of each profile. The dotted contour lines show the estimated morphologies of the subducted South China Sea slab (SCSs), the proto South China Sea slab (PSCSs), the Philippine Sea slab (PSs), the Sulu Sea slab (SSs) and the Molucca Sea slab (MSs) along the Manila Trench (MT), the Philippine Trench (PT), the Negros Trench (NT) and the Sangihe Trench (ST), respectively. The horizontal red dashed lines denote the 410 and 660 km discontinuities. CT, the Cotabato Trench; ELT, the East Luzon Trough; ELTF, the East Luzon Transform Fault. The other symbols are the same as those in Fig. 1.

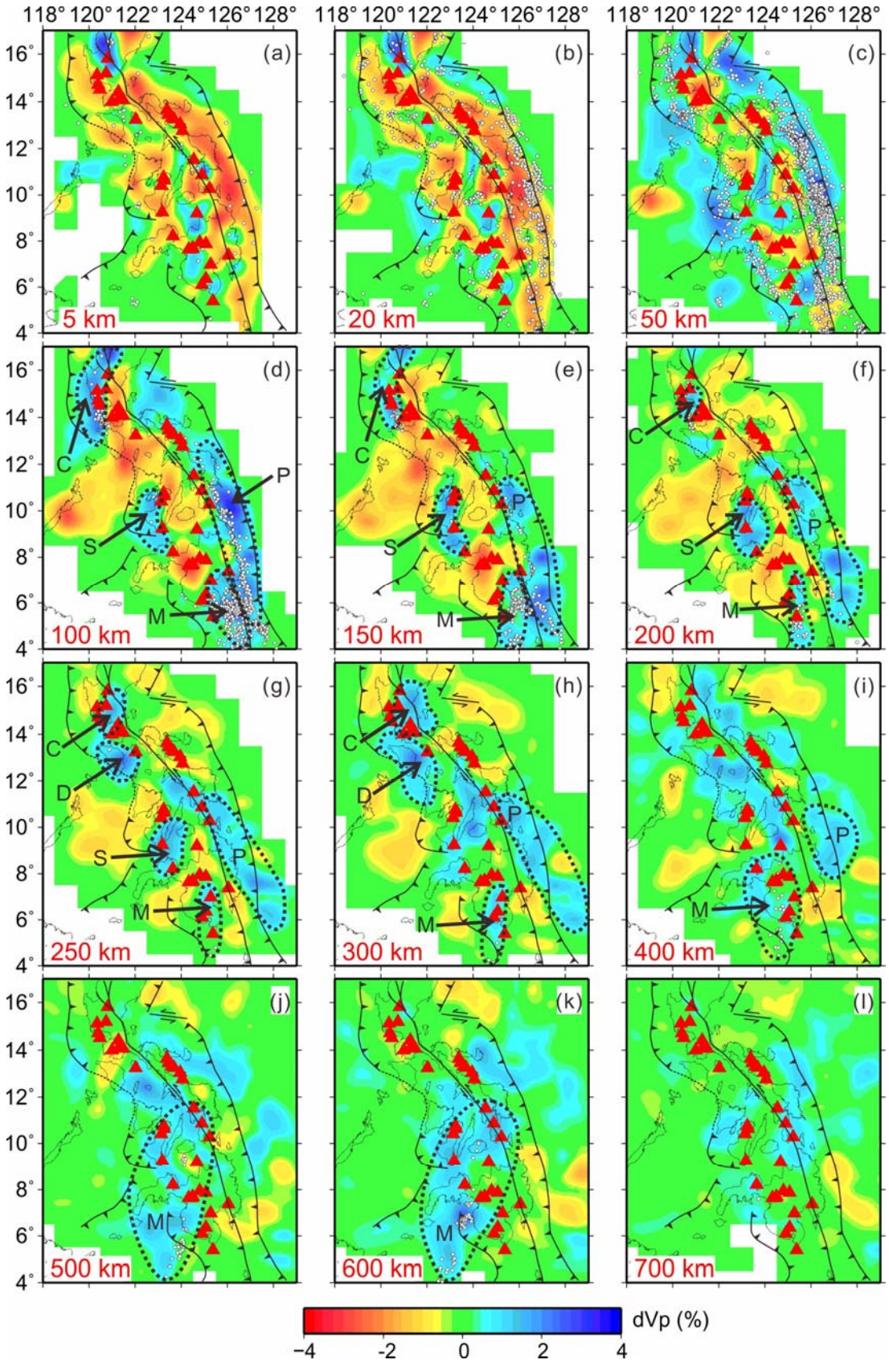
118° 120° 122° 124° 126° 128°
16° 14° 12° 10° 8° 6° 4°
(a)
5 km
(b)
20 km
(c)
50 km
(d)
C
P
S
M
100 km
(e)
150 km
(f)
200 km
(g)
D
250 km
(h)
300 km
(i)
400 km
(j)
500 km
(k)
600 km
(l)
700 km
dVp (%)
−4 -2 0 2 4

Fig. 4. Map views of isotropic Vp tomography. The layer depth is shown at the lower-left corner of each map. The red triangles denote active volcanoes. The red and blue colors denote slow and fast Vp perturbations, respectively, whose scale is shown at the bottom. The dotted contour lines show the estimated morphologies of the subducted South China Sea slab (C), the detached South China Sea slab (D), the Philippine Sea slab (P), the Sulu Sea slab (S) and the Molucca Sea slab (M). The other symbols are the same as those in Fig. 1.

Two kinds of synthetic tests are performed to evaluate the spatial resolution of the isotropic Vp tomographic images: the checkerboard resolution tests (CRTs) and the restoring resolution tests (RRTs) (Zhao, 2015). In the CRT, an input checkerboard model is firstly constructed with Vp perturbations of ±4% at adjacent grid nodes, then synthetic travel times are calculated for the checkerboard model with the same distribution of seismic stations and earthquakes as those in the observed data set. Gaussian random noise with a standard deviation of 0.1 s is added to the synthetic data to simulate the data errors. Then an output model is obtained by inverting the synthetic data to estimate the resolution of the tomographic images. Lévěque et al. (1993) showed that for a tomographic result, sometimes a smaller-scale structure may have a good resolution, but larger-structures may not be well retrieved. To investigate if our result has such a problem, we calculated two CRTs with different grid intervals. Figs. S3 and S4 show the obtained CRT results with lateral grid intervals of 0.6° and 1.0°, respectively, which indicate that the input Vp models are well recovered in both of the tests. The CRT results are consistent with the distribution of the P-wave ray paths (Fig. S5).

To further confirm the robustness of our tomographic results, a RRT is conducted. The RRT is the same as the CRT except that its input model is derived from the obtained Vp tomography (Figs. 3 and 4). The RRT results (Fig. S6) show that main features of our tomographic model can be recovered very well at all depths, though slight smearing occurs at the edge parts.

4. Azimuthal anisotropy tomography

P-wave azimuthal anisotropy tomography is conducted by using the method of Wang and Zhao (2008). For weak azimuthal anisotropy with a horizontal hexagonal symmetry, P-wave slowness can be approximately expressed as (e.g., Backus, 1965; Hearn, 1996; Eberhart-Phillips and Henderson, 2004; Wang and Zhao, 2008, 2013):

$$S(\emptyset) = S_0(1 + A\cos(2\emptyset) + B\sin(2\emptyset)). \quad (1)$$

where S is the total slowness, S_0 is the isotropic slowness, A and B are azimuthal anisotropy parameters, and $\emptyset$ is ray path azimuth. The fast-velocity direction (FVD) and the amplitude of azimuthal anisotropy can be expressed as follows:

$$\psi=\begin{cases}\frac{1}{2}tan^{-1}\left(\frac{B}{A}\right)+\begin{cases}\frac{\pi}{2}, & A>0\\ 0, & A<0,\end{cases}\\ -\frac{\pi}{4}, \quad A=0, \quad B>0,\\ \frac{\pi}{4}, \quad A=0, \quad B<0,\end{cases} \tag{2}$$

$$\alpha=\frac{V_{fast}-V_{slow}}{2V_0}=\frac{\sqrt{A^2+B^2}}{1-(A^2+B^2)},$$

where V_0 is average isotropic velocity, and V_{fast} and V_{slow} are P-wave velocities in the fast and slow directions, respectively.

For Vp anisotropic tomography, a good coverage of rays in azimuth and incident angle is required. Hence, a sparser 3-D grid is adopted to express Vp azimuthal anisotropy, and meshes of grid nodes are set with a lateral grid interval of 1.2° and at depths of 5, 20, 50, 100, 150, 250, 400 and 600 km in the crust and upper mantle. The optimal values of the damping and smoothing parameters are found to be 100 and 2000, respectively (Fig. S7) for the Vp azimuthal anisotropy tomography.

To evaluate the resolution and robustness of our azimuthal anisotropy tomography, we conducted three CRTs with different values of the isotropic Vp and azimuthal anisotropy parameters in the input models: 1) with the isotropic Vp perturbations of ±4% and the anisotropic parameter (A and B) perturbations of ±3%; 2) no isotropic Vp perturbation but with the anisotropic parameter (A and B) perturbations of ±3%; and 3) with the isotropic Vp perturbations of ±4% but without azimuthal anisotropy. Gaussian random noise with a standard deviation of 0.1 s is added to the synthetic data calculated from the input model. In the CRTs, the ±3% perturbations of A and B result in azimuthal anisotropies with an amplitudes of 4.25% and FVDs of 112.5° and 22.5°, respectively. Figs. S8-S13 show the CRT results with lateral grid intervals of 0.6° and 1.0° for the isotropic Vp and lateral grid intervals of 1.2° and 1.5° for the azimuthal anisotropy, respectively. The resolution of isotropic Vp image (Figs. S8 and S11) is generally consistent with that of the isotropic tomography (Figs. S3 and S4). For the azimuthal anisotropy, the resolution is high only beneath the Philippine Islands and their offshore areas above 150 km depth. Below 250 km depth, although the input model is not well recovered, the input and output FVDs are roughly consistent (Figs. S8 and S11).

We also conducted CRTs to evaluate the trade-off between the isotropic Vp and azimuthal anisotropy (Figs. S9, S10, S12 and S13). The results show that the input models can be well recovered and the trade-off effect is generally very small, though there are some artefacts at the margin of the study region due to poor ray coverage. These test results indicate that the isotropic Vp and azimuthal anisotropy have a lateral resolution of 0.6° and 1.2°, respectively, and the trade-off between the isotropic Vp and the azimuthal anisotropy is insignificant. After the azimuthal anisotropy inversion, the P-wave RMS travel-time residual is reduced to 0.840 s.

Fig. 5 shows the results of Vp azimuthal anisotropy tomography in the study region. The isotropic Vp pattern is quite consistent with that obtained by the isotropic inversion (Fig. 4). The anisotropic patterns are complex in the crust and upper mantle. The FVDs in the crust and uppermost mantle (Fig. 5a-5c) are roughly parallel with the strikes of major tectonic features, i.e., the Philippine Fault and the trenches, mainly attributing to the active faults and cracks resulted from the plate subductions (e.g., Koulakov et al., 2015; Zhao et al., 2016). The subducted SCS slab exhibits trench-parallel FVDs (Fig. 5d), similar to that revealed in the Hikurangi subduction zone beneath the central North Island, New Zealand (Eberhart-Phillips and Reyners, 2009), which roughly perpendicular to the magnetic lineations in the SCS (e.g., Taylor and Hayes, 1983; Briais et al., 1993), suggesting that the slab keeps its frozen-in anisotropy formed at the mid-ocean ridge (e.g., Wang and Zhao, 2013). The FVDs are approximately trench-parallel in the subducted PHS slab north of ~10°N, but trench-normal in the PHS slab south of ~10°N (Fig. 5d), which are almost parallel with and perpendicular to the magnetic lineations in the West Philippine Basin and the Palau Basin, respectively (e.g., Taylor and Goodliffe, 2004; Sasaki et al., 2014). The trench-parallel and trench-normal FVDs are presumably caused by LPO of the B-type olivine or original fossil anisotropy in the slab formed at the mid-ocean ridge (e.g., Zhao et al., 2016). In the upper mantle below 250 km depth and the MTZ (Fig. 5f-5h), the FVDs change gradually from NE-SW to NW-SE northwards. This result is consistent with a previous model of Vp azimuthal anisotropy (Huang et al., 2015), possibly indicating a mantle flow in and around the MTZ, and coinciding with high-pressure experiments on seismic anisotropy in the MTZ (e.g., Tommasi et al., 2004; Wang et al., 2006; Mainprice et al., 2007; Miyagi et al., 2014; Tsujino et al., 2016).

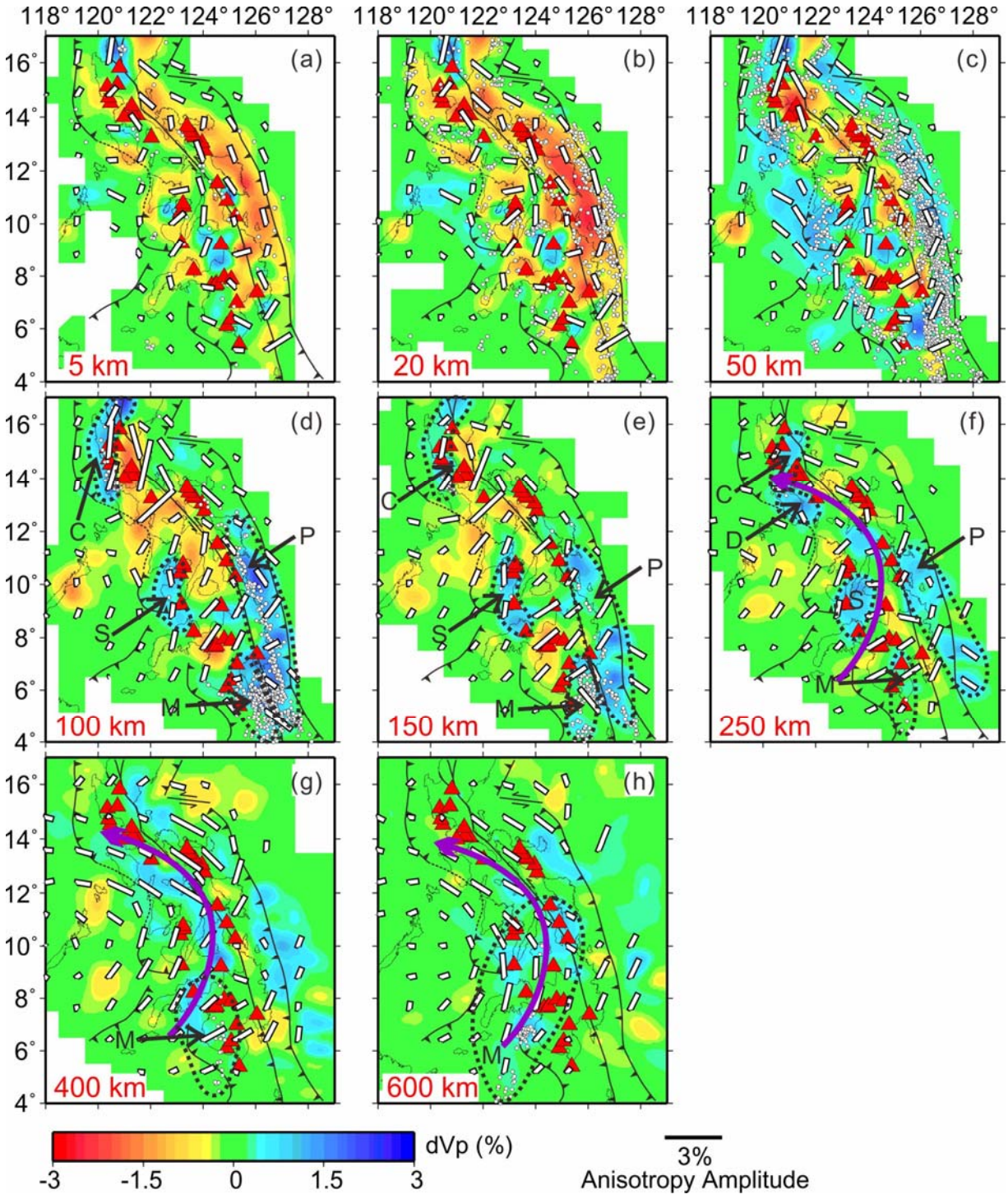

Fig. 5. Map views of P-wave azimuthal anisotropy tomography. The layer depth is shown at the lower-left corner of each map. The red and blue colors denote low and high isotropic Vp perturbations, respectively. The orientation and length of the white bars represent the fast-velocity direction and the amplitude of azimuthal anisotropy, respectively. The scales for the isotropic Vp and anisotropy are shown at the bottom. The red

triangles denote active volcanoes. The purple arrows indicate the possible mantle flow directions. The dotted contour lines show the estimated morphologies of the subducted South China Sea slab (C), the detached South China Sea slab (D), the Philippine Sea slab (P), the Sulu Sea slab (S) and the Molucca Sea slab (M). The other symbols are the same as those in Fig. 1.

To further evaluate the reliability of the azimuthal anisotropy tomography, we conducted several RRTs with different input models. The test results (Figs. S14-S19) show that the input anisotropic patterns (especially that of FVDs) are generally well recovered, suggesting that our azimuthal anisotropy tomography is quite reliable.

5. Radial anisotropy tomography

The method of Wang and Zhao (2013) is applied to conduct 3-D Vp radial anisotropy (RAN) tomography, which is based on the assumption of weak RAN. P-wave slowness in such a medium can be expressed as follows:

$$S = S_0[1 + Mcos(2i)] \quad (3)$$

where i is incident angle of a ray, and M is RAN parameter. The RAN amplitude can be expressed as:

$$\beta = \frac{V_{ph}-V_{pv}}{2V_0} = \frac{M}{1-M^2}, \quad (4)$$

where V_0 is the isotropic Vp; V_{ph} and V_{pv} are P-wave velocities in the horizontal and vertical directions, respectively. $\beta > 0$ means that the horizontal Vp is greater than the vertical Vp, i.e., $V_{ph} > V_{pv}$, whereas $\beta < 0$ means that the horizontal Vp is smaller than the vertical Vp, i.e., $V_{ph} < V_{pv}$.

For the RAN tomography, meshes of grid nodes are set with a lateral grid interval of 1.2° and at depths of 5, 20, 50, 100, 150, 200, 250, 300, 400, 500 and 650 km in the crust and upper mantle under the study region. The optimal values of damping and smoothing parameters are found to be 100 and 2000, respectively (Fig. S20) for the Vp RAN tomography.

Similar to the CRTs for the azimuthal anisotropy tomography, three CRTs are conducted with different values of the isotropic Vp and RAN parameters in the input models: 1) with ±4% perturbations to the isotropic Vp and ±4% perturbations to the RAN parameter; 2) no isotropic

Vp perturbation but with ±4% perturbations to the RAN parameter; and 3) with isotropic Vp perturbations of ±4% but without RAN. Gaussian random noise with a standard deviation of 0.1 s is also added to the synthetic data calculated from the input models. Figs. S21-S26 show the CRT results with lateral grid intervals of 0.6° and 1.0° for the isotropic Vp and lateral grid intervals of 1.2° and 1.5° for the RAN. The resolution of the isotropic Vp image (Figs. S21 and S24) is good at most depths beneath the Philippine Islands except for 650 km depth, which is generally concordant with that of the isotropic Vp tomography (Figs. S3 and S4). For the RAN, the resolution is high beneath the Philippine Islands and their offshore areas at depths of 5 to 500 km, whereas at 650 km depth, the input model is well recovered in the southern part of the study region (Figs. S21 and S24).

We also conducted CRTs to evaluate the trade-off between isotropic Vp and RAN (Figs S22-S23, S25-S26). The test results show that when either the isotropic Vp or RAN is considered in the input model, the other part shows up in the output model with a small amplitude, though there are some artefacts at the edges of the study region due to poor ray coverage there. These CRTs suggest that the isotropic Vp and RAN have a lateral resolution of 0.6° and 1.2°, respectively, and the trade-off between the isotropic Vp and the RAN is insignificant. After the RAN inversion, the RMS travel-time residual is reduced to 0.831 s.

Fig. 6 shows vertical cross-sections of Vp RAN tomography along seven profiles. The isotropic Vp image is similar to that determined by the isotropic inversion (Fig. 3). The RAN in the high-V subducted slabs is generally negative, i.e., $V_{pv} > V_{ph}$, probably due to the near-vertical slab subductions, similar to the results in the Alps region (Hua et al., 2017). The RAN in the subducted Sulu Sea slab above 100 km depth and the PHS slab above 150 km depth is positive (Fig. 6d and 6e), similar to the Vp RAN results of the Japan subduction zone (e.g., Niu et al., 2016; Liu and Zhao, 2017; Gou et al., 2018), which may suggest that the two slabs keep their frozen-in anisotropy formed at the mid-ocean ridge, or the slab anisotropy is induced by LPO of the B-type olivine generated by mantle flow or topotactic growth of the aligned antigorite (e.g., Nagaya et al., 2014, 2016; Zhao et al., 2016). The RAN within the subducted slabs has a larger amplitude than that in the mantle above or beneath the slabs, suggesting that the subducted slabs may be the primary sources of seismic anisotropy (Eberhart-Phillips and Reyners, 2009). The low-V anomalies under the active volcanoes also exhibit a negative RAN (i.e., $V_{pv} > V_{ph}$), possibly reflecting hot upwelling flows and transitions of olivine fabrics in the

mantle wedge due to the dehydration of the subducted slabs (e.g., Zhao et al., 2016; Liu and Zhao, 2017). The low-V zones between the Manila Trench and the Philippine Trench in profiles A-C (Fig. 6a-6c) generally exhibit a positive RAN (i.e., $V_{pv} < V_{ph}$), suggesting the existence of a horizontal mantle flow there. The RAN results show $V_{pv} < V_{ph}$ in the low-V anomalies between the Molucca Sea and the Philippine Sea slabs (Fig. 6g), which may also suggest the existence of a horizontal mantle flow between the two slabs. In the MTZ, a positive RAN (i.e., $V_{pv} < V_{ph}$) is revealed (Fig. 6), which, together with the azimuthal anisotropy (Fig. 5g and 5h), indicate a horizontal mantle flow there.

Four RRTs with different input models (Figs. S27-S30) are performed to investigate the reliability of our RAN tomography. The RRT results show that the above-mentioned major RAN results are quite robust.

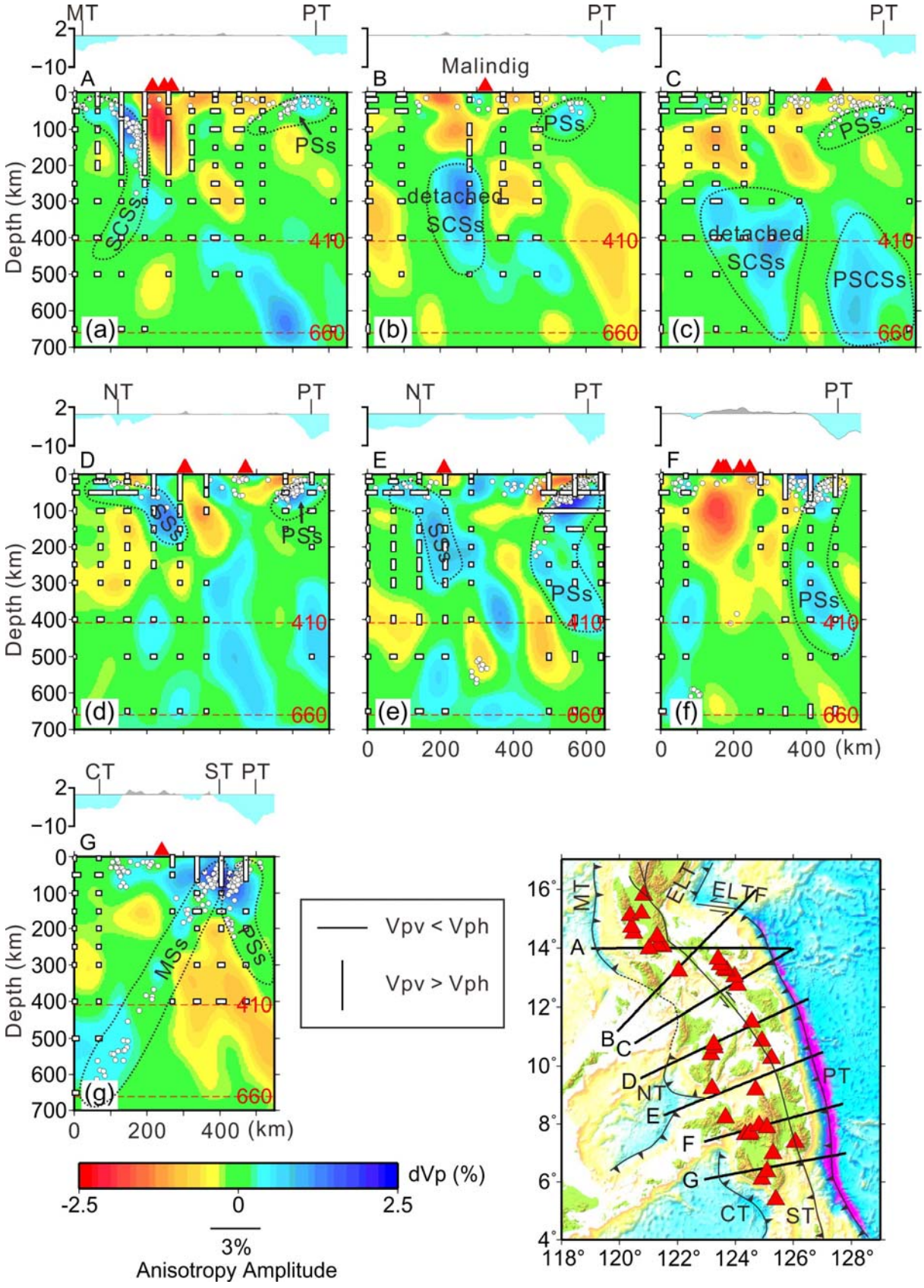
MT
PT
A
B
C
Malindig
PSs
SCSs
detached
PSCSs
410
660
(a)
(b)
(c)
Depth (km)
NT
D
E
F
(d)
(e)
(f)
0
200
400
600
(km)
CT
ST
G
MSs
(g)
Vpv < Vph
Vpv > Vph
dVp (%)
-2.5
2.5
3%
Anisotropy Amplitude
ELT
16°
14°
12°
10°
8°
6°
4°
118°
120°
122°
124°
126°
128°

Fig. 6. Results of P-wave radial anisotropy tomography along seven vertical profiles shown on the inset map. The red and blue colors represent low and high isotropic Vp perturbations, respectively, whose scale is shown at the bottom-left. The horizontal and vertical white bars represent $V_{ph} > V_{pv}$ and $V_{ph} < V_{pv}$, respectively. The length of the bars denotes the amplitude of radial anisotropy, whose scale is also shown at the bottom-left. The white dots and red triangles show local earthquakes and active volcanoes, respectively, within a 30-km width of each profile. The dotted contour lines show the estimated morphologies of the subducted South China Sea slab (SCSs), the proto South China Sea slab (PSCSs), the Philippine Sea slab (PSs), the Sulu Sea slab (SSs), the Celebes Sea slab (CSs) and the Molucca Sea slab (MSs) along the Manila Trench (MT), the Philippine Trench (PT), the Negros Trench (NT), the Cotabato Trench (CT) and the Sangihe Trench (ST), respectively. The horizontal red dashed lines denote the 410 and 660 km discontinuities. ELT, the East Luzon Trough; ELTF, the East Luzon Transform Fault. The other symbols are the same as those in Fig. 1.

6. Discussion

6.1 Morphologies of the subducted slabs

Our tomographic results uncover general morphologies of the three subducted slabs in the study region, which are well concordant with previous works (e.g., Fan et al., 2017; Fan and Zhao, 2018). The SCS slab has subducted to ~450 km depth with an overturned dipping angle above the MTZ (Fig. 3a), similar to the subducted PHS slab (Fig. 3e and 3f), whereas the subducted Molucca Sea slab dips straightforwardly down to ~650 km depth (Fig. 3g). The diverse morphologies of these slabs may be resulted from different tectonic settings and dynamic mechanisms.

The steepening and detachment of the SCS slab, which are also testified by chemical and isotopic evidence from the volcanoes above the subducted SCS slab (Ku et al., 2009), may be due to the collision between the Palawan block and the Philippine Mobile Belt. A 3-D numerical modeling study (Menant et al., 2016) shows that in a subduction zone, when colliding with the trench, a continental lithosphere would separate apart from the subducted oceanic lithosphere along their interaction zone due to the buoyance of the continental lithosphere, which further benefits the formation of asthenospheric flow through the slab window. The asthenospheric flow facilitates the subducted oceanic lithosphere beside the continental lithosphere weakening and

bending (Lallemand et al., 2005). In addition, the collision between the continental and the oceanic lithospheres favors partial decoupling between the subducted oceanic plate and the overriding plate (Menant et al., 2016), both of which may give rise to the increase of the dipping angle of the SCS slab.

Numerical simulations (Holt et al., 2017) show that in the case of two slabs dipping in the same direction, the subduction of the front slab (the Molucca Sea slab in the present case) can cause a positive pressure difference between the lower and upper surfaces of the rear slab (the PHS slab; Fig. 7), which would produce a horizontal mantle flow to push the rear slab backwards to fold into an overturned geometry. This scenario can explain our RAN tomographic results (Figs. 3e-3g and 6e-6g). In addition, similar outcomes exist when two plates subduct towards each other (Holt et al., 2017). Hence, the subduction of the Sulu Sea slab may partly affect the dip angle of the PHS slab.

The complete subduction of the Molucca Sea slab brings about uncertainties of the age and other attributes of the Molucca Sea plate. A total length of 1500 to 1600 km of subducted lithosphere is estimated on the basis of global tomography (e.g., Hall and Spakman, 2015), which comprises 900-950 km subducted slab with an average dip of 45° along the Sangihe Trench (Figs. 3g and 6g) and 400-450 km subducted slab with a similar average dip along the Halmahera Trench. Both seismic observations and numerical simulations suggest that, due to the phase transition, the positive buoyancy forces near the 660 km discontinuity (ringwoodite to bridgmanite and periclase), instead of the 410 km discontinuity (olivine to wadsleyite), are sufficient to resist the slab subduction (e.g., Fukao and Obayashi, 2013; Agrusta et al., 2017). During its subduction, the Molucca Sea slab may be not affected by other factors, such as the PHS slab subduction, to maintain the status revealed by our tomography (Figs. 3g and 6g), which is distinct from the subduction of the SCS and PHS slabs.

6.2 Subduction initiation along the northern Philippine Trench

Subduction initiation (SI) is a key and essential part of global plate tectonics. To data, great progress has been made in the SI-related research, and many mechanisms for SI have been proposed (Stern and Gerya, 2017 and references therein). The Philippine Trench marks a young subduction zone, and different models for its origin and evolution have been presented. Cardwell et al. (1980) suggested that the subduction along the Philippine Trench started from the north to

the south (Pubellier et al., 1996; Ozawa et al., 2004), whereas Lallemand et al. (1998) proposed that the subduction at the Philippine Trench initiated at its central segment, and then propagated toward both the north and the south (Fan et al., 2017). A recent study of seismic tomography suggests the earliest SI along the Philippine Trench at its southern segment (Fan and Zhao, 2018). Despite of these different models, it is unanimous that SI along the northern Philippine Trench was induced by the collision between the Palawan block and the Philippine Mobile Belt before 8-9 Ma (Marchadier and Rangin, 1990). However, the dynamical mechanism remains enigmatic. Our anisotropic tomography provides new constraints on the SI mechanism along the northern Philippine Trench.

It is generally accepted that SI by forces associated with plate tectonics is very difficult and requires lithospheric-scale weak zones, which should either be inherited from previous plate tectonic history or develop self-consistently during SI in the strong plate interior due to various rheological feedback mechanisms (Stern and Gerya, 2017 and references therein). Our anisotropic tomography reveals that a horizontal mantle flow exists beneath the northern Philippine Trench (Fig. 6a-6c), which could be ascribed to the slab tearing resulted from the collision between the Palawan block and the Philippine Mobile Belt, as well as the subduction and roll-back of the South China Sea slab. The induced horizontal mantle flow has been testified by 3-D numerical models (Menant et al., 2016), which show that in a subduction zone, the collision between the continental lithosphere with the trench results in slab tearing and asthenospheric flow above the detached slab. Our tomographic images coincide well with the numerical models. The horizontal flow engenders the formation of additional stresses in the lithosphere, which is comparable with the critical yield stress required for SI by plate forces and with the estimates of stresses in the subduction zone (Solomatov, 2004). According to the previous tomographic studies (Fan et al., 2015, 2017), the maximum depth of the subducted Philippine Sea slab along the East Luzon Trough and the Philippine Trench is ~100 km, indicating that the two trenches presumably initiated at the same time as one subduction system and then separated due to the approach of the Benham Rise at ~3.2 Ma (Bautista et al., 2001). Considering that the East Luzon Trough and the Luzon-Okinawa Fracture Zone are in alignment (Fig. 1), it can be inferred that the Philippine Trench was transformed from the pre-Luzon-Okinawa Fracture Zone, due to the northwestward movement of the Philippine Sea Plate and the

collision between the Palawan block and the Philippine Mobile Belt, where the horizontal flow facilitates the SI along the northern Philippine Trench.

6.3 Origin of the Indian-type mantle under eastern South China Sea

The South China Sea is surrounded by the Eurasian, the Australian and the Philippine Sea plates, which is a northern hemispheric marginal basin formed by rifting of the Eurasian continent between 33-15.5 Ma (Taylor and Hayes, 1983; Briais et al., 1993; Li et al., 2014). A recent geochemical study has revealed that basalts of the South China Sea are Indian-type mid-ocean ridge basalts (Zhang et al., 2018), which are known to originate from the upper mantle of the southern hemisphere (Dupré and Allègre, 1983; Hart, 1984, 1988). The genesis of the Indian-type mantle under the South China Sea is thought to be in situ and ascribed to the combined influence of the Hainan plume and recycling of the lower continental crust (Zhang et al., 2018). Our anisotropic tomography sheds new light on the origin of the Indian-type mantle beneath the eastern part of the South China Sea.

Our tomographic results indicate the existence of anisotropy in the MTZ, where wadsleyite and ringwoodite are the dominant mineral phases in the upper (410-520 km) and lower (520-660 km) parts of the MTZ, respectively. LPO of wadsleyite is widely accepted to be the main source of anisotropy in the upper MTZ (e.g., Tommasi et al., 2004), whereas there are three candidates for the anisotropy in the lower MTZ. The first is the plastic anisotropy of ringwoodite, which has been observed by high shear-strain deformation experiments (e.g., Miyagi et al., 2014), but the amount of anisotropy of ringwoodite is too small to produce significant seismic anisotropy in the lower MTZ (e.g., Li et al., 2006; Wang et al., 2006). The second candidate is the deformation-induced LPO of bridgmanite, the dominant constituent of the lower mantle, which is testified by shear deformation experiments to be the most important source of anisotropy in the uppermost lower mantle, but it would require a 1000-2000 km subducted slab region (Tsujino et al., 2016). The third candidate is the fabrics of the hydrous D phase, a dense hydrous magnesium silicate phase, which was calculated by Mainprice et al. (2007) suggesting that the hydrous D phase might be the main source of anisotropy in the lower MTZ with deep slab penetration in a subduction zone (Di Leo et al., 2012).

Our results suggest the existence of horizontal mantle flow in and above the MTZ between the Celebes-Molucca seas and the eastern South China Sea (Figs. 5f-5h and 6a-6f), which is

consistent with the recent shear-wave splitting measurements by Di Leo et al. (2012, 2014). They investigated the anisotropic structure of the Sangihe subduction zone with shear-wave splitting measurements of local S and SKS phases at two stations, as well as downgoing S phases at five stations at teleseismic distances. Their results suggest that the mantle flow is induced by the simultaneous westward and eastward subduction of the Molucca Sea slab, indicating lateral escape of mantle beneath the Molucca Sea slab (Di Leo et al., 2012, 2014). Combining the shear-wave splitting results with our Vp anisotropic tomography, we deem that the mantle escapes from the Molucca Sea and the Celebes Basin into the eastern South China Sea with the Indian-type mantle material.

However, the eastward SI of the Molucca Sea slab was around 7 Ma ago (Elburg and Foden, 1998), indicating that the lateral mantle flow under the Molucca Sea would not initiate earlier than 7 Ma, which is inconsistent with the ages of the Indian-type basalts in the eastern South China Sea (~12.8-7.4 Ma, Zhang et al., 2017). Therefore, the mantle flow resulted from the double-side subduction of the Molucca Sea slab may not be the contributor to the Indian-type mantle in the eastern South China Sea. Numerical simulations have shown that the horizontal mantle flow can occur when two plates subduct in the same direction (e.g., Holt et al., 2017). Since ~20 Ma, both the Moucca Sea and the Philippine Sea plates have subducted westwards (Fig. 6g, Fan and Zhao, 2018), resulting in the upper mantle between the two slabs moving northwards due to the block of the subducted Australian plate in the south. Meanwhile, spreading of the South China Sea requires a great deal of magmatic supply, inducing the mantle flow from the Molucca Sea into the eastern South China Sea (Fig. 7). From the above discussions, it can be speculated that the Celebes, the Sulu and the South China seas may all contain basalts of the Indian-type mantle.

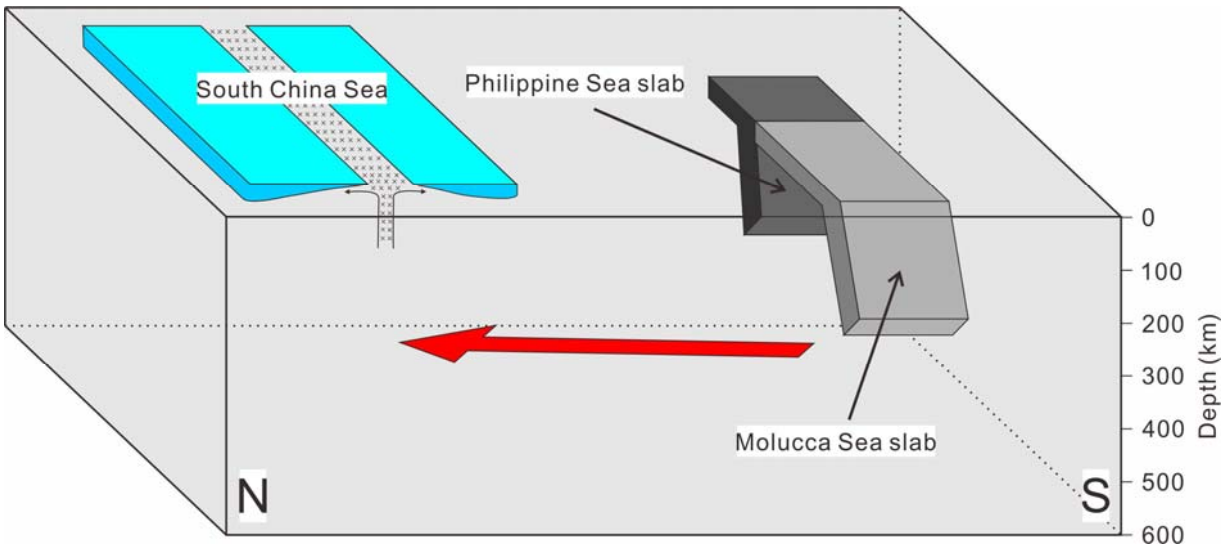

Fig. 7. A schematic diagram illustrating a possible origin of the Indian-type mantle beneath the eastern South China Sea.

7. Conclusions

The first 3-D model of P-wave azimuthal and radial anisotropy tomography beneath the central and southern Philippines is determined by inverting a large number of P-wave arrival-time data of local and teleseismic events. Our results suggest that a horizontal mantle flow exists between the Manila Trench and the Philippine Trench, which is induced by the collision between the Palawan block and the Philippine Mobile Belt, as well as roll-back of the South China Sea slab. The horizontal mantle flow facilitates the subduction initiation along the northern part of the Philippine Trench, which may be transformed from the pre-Luzon-Okinawa Fracture Zone, due to the northwestward movement of the Philippine Sea Plate and the collision between the Palawan block and the Philippine Mobile Belt. A horizontal mantle flow also exists in and above the mantle transition zone beneath the central and southern Philippines, suggesting that basalts of the Indian-type mantle in the eastern part of the South China Sea probably originated from the mantle beneath the Celebes and Molucca seas.

Acknowledgements

We appreciate the constructive comments and suggestions from the Editor (Prof. Vernon Cormier) and two anonymous referees. This work was financially supported by the National Natural Science Foundation of China (grant 41876043) and the National Special Project for

Global Change and Air-Sea Interaction (GASI-GEOGE-02) to J. Fan, as well as research grants from Japan Society for the Promotion of Science (Kiban-S 23224012) and the Japanese Ministry of Education, Culture, Sports, Science and Technology (MEXT, Shin-Gakujutsu 26106005) to D. Zhao. Most of the figures are made using the GMT software package (Wessel and Smith, 1998).

References

Agrusta, R., Goes, S., van Hunen, J., 2017. Subducting-slab transition-zone interaction: Stagnation, penetration and mode switches. Earth Planet. Sci. Lett. 464, 10-23.

Backus, G.E., 1965. Possible forms of seismic anisotropy of the uppermost mantle under oceans. J. Geophys. Res. 70(14), 3429-3439.

Bautista, B.C., Bautista, M.L.C., Oike, K., Wu, F.T., Punongbayan, R.S., 2001. A new insight on the geometry of subducting slabs in northern Luzon, Philippines. Tectonophysics 339, 279-310.

Briais, A., Patriat, P., Tapponnier, P., 1993. Updated interpretation of magnetic anomalies and seafloor spreading stages in the South China Sea: Implications for the Tertiary tectonics of Southeast Asia. J. Geophys. Res. 98(B4), 6299-6328.

Cardwell, R.K., Isacks, B.L., Karig, D.E., 1980. The spatial distribution of earthquakes, focal mechanism solutions, and subducted lithosphere in the Philippine and northern Indonesian islands. Am. Geophys. Union Monogr. 23, 1-35.

Castillo, P.R., Janney, P.E., Solidum, R., 1999. Petrology and geochemistry of Camiguin Island, southern Philippines: Insights to the source for adakite and other lavas in a complex arc tectonic setting. Contrib. Mineral. Petrol. 134, 33-51.

Di Leo, J.F., Wookey, J., Hammond, J., Kendall, J.M., Kaneshima, S., Inoue, H., Yamashina, T., Harjadi, P., 2012. Deformation and mantle flow beneath the Sangihe subduction zone from seismic anisotropy. Phys. Earth Planet. Inter. 194-195, 38-54.

Di Leo, J.F., Walker, A.M., Li, Z.H., Wookey, J., Ribe, N.M., Kendall, J.M., Tommasi, A., 2014. Development of texture and seismic anisotropy during the onset of subduction. Geochem. Geophys. Geosyst. 15, 192-212.

Dupré, B., Allègre, C.J., 1983. Pb-Sr isotope variation in Indian Ocean basalts and mixing phenomena. Nature 303, 142-146.

Eberhart-Phillips, D., 1986. Three-dimensional velocity structure in northern California Coast Ranges from inversion of local earthquake arrival times. Bull. Seismol. Soc. Am. 76, 1025-1052.

Eberhart-Phillips, D., Henderson, C.M., 2004. Including anisotropy in 3-D velocity inversion and application to Marlborough, New Zealand. Geophys. J. Int. 156(2), 237-254.

Eberhart-Phillips, D., Reyners, M., 2009. Three-dimensional distribution of seismic anisotropy in the Hikurangi subduction zone beneath the central North Island, New Zealand. J. Geophys. Res., 114, B06301.

Elburg, M., Foden, J., 1998. Temporal changes in arc magma geochemistry, northern Sulawesi, Indonesia. Earth Planet. Sci. Lett. 163, 381-398.

Engdahl, E.R., van der Hilst, R., Buland, R., 1998. Global teleseismic earthquake relocation with improved travel times and procedures for depth determination. Bull. Seismol. Soc. Am. 88, 722-743.

Engdahl, E.R., 2006. Application of an improved algorithm to high precision relocation of ISC test events. Phys. Earth Planet. Inter. 158, 14-18.

Fan, J., Wu, S., Spence, G., 2015. Tomographic evidence for a slab tear induced by fossil ridge subduction at Manila Trench, South China Sea. Int. Geol. Rev. 57, 998-1013.

Fan, J., Zhao, D., Dong, D., Zhang, G., 2017. P-wave tomography of subduction zones around the central Philippines and its geodynamic implications. J. Asian Earth Sci. 146, 76-89.

Fan, J., Zhao, D., 2018. Evolution of the southern segment of the Philippine Trench: Constraints from seismic tomography. Geochem. Geophys. Geosyst. 19. https://doi.org/10.1029/2018GC007685.

Fouch, M., Rondenay, S., 2006. Seismic anisotropy beneath stable continental interiors. Phys. Earth Planet. Inter. 158, 292-320.

Fukao, Y., Obayashi, M., 2013. Subducted slabs stagnant above, penetrating through, and trapped below the 660km discontinuity. J. Geophys. Res. 118, 5920-5938.

Global Volcanism Program, 2013. Volcanoes of the World, v. 4.6.7. Venzke, E (ed.). Smithsonian Institution. Downloaded 02 Apr 2018. https://dx.doi.org/10.5479/si.GVP.VOTW4-2013.

Gou, T., Zhao, D., Huang, Z., Wang, L., 2018. Anisotropic 3-D ray tracing and its application to Japan subduction zone. J. Geophys. Res. 123, 4088-4108.

Hall, R., Spakman, W., 2015. Mantle structure and tectonic history of SE Asia. Tectonophysics 658, 14–45.

Hart, S.R., 1984. A large-scale isotope anomaly in the Southern Hemisphere mantle. Nature 309, 753-757.

Hart, S.R., 1988. Heterogeneous mantle domains: signatures, genesis and mixing chronologies. Earth Planet. Sci. Lett. 90(3), 273-296.

Hearn, T.M., 1996. Anisotropic Pn tomography in the western United States. J. Geophys. Res. 101(B4), 8403-8414.

Holt, A.F., Royden, L.H., Becker, T.W., 2017. The dynamics of double slab subduction. Geophys. J. Int. 209, 250-265.

Hua, Y., Zhao, D., Xu, Y., 2017. P wave anisotropic tomography of the Alps. J. Geophys. Res. 122(6), 4509-4528.

Huang, Z., Zhao, D., Wang, L. 2015. P wave tomography and anisotropy beneath Southeast Asia: Insight into mantle dynamics. J. Geophys. Res. 120(7), 5154-5174.

Kennett, B.L.N., Engdahl, E.R., 1991. Traveltimes for global earthquake location and phase identification. Geophys. J. Int. 105, 429-465.

Koulakov, I., Kukarina, E., Fathi, I., Khrepy, S., Al-Arifi, N., 2015. Anisotropic tomography of Hokkaido reveals delamination-induced flow above a subducting slab. J. Geophys. Res. 120, 3219-3239.

Ku, Y.P., Chen, C.H., Song, S.R., Iizuka, Y., Shen, J.J.S., 2009. A 2 Ma record of explosive volcanism in southwestern Luzon: implications for the timing of subducted slab steepening. Geochem. Geophys. Geosyst. 10, Q06017.

Lallemand, S., Popoff, M., Cadet, J.P., Bader, A.G., Pubellier, M., Rangin, C., Deffontaines, B., 1998. Genetic relations between the central and southern Philippine trench and the Sangihe trench. J. Geophys. Res. 103, 933-950.

Lallemand, S., Heuret, A., Boutelier, D., 2005. On the relationships between slab dip, back-arc stress, upper plate absolute motion, and crustal nature in subduction zones. Geochem. Geophys. Geosyst. 6(9), Q09006.

Laske, G., Masters, G., Ma, Z., Pasyanos, M., 2013. Update on CRUST1.0 - A 1-degree Global Model of Earth's Crust. Geophys. Res. Abstracts 15, Abstract EGU, 2013-2658.

Lévěque, J., Rivera, L., Wittlinger, G., 1993. On the use of the checker-board test to assess the resolution of tomographic inversions. Geophys. J. Int. 115, 313–318.

Li, C.F. et al., 2014. Ages and magnetic structures of the South China Sea constrained by deep tow magnetic surveys and IODP Expedition 349. Geochem. Geophys. Geosyst. 15, 4958-4983.

Li, L., Weidner, D.J., Brodholt, J., Alfè, D., Price, G.D., 2006. Elasticity of Mg_2SiO_4 ringwoodite at mantle conditions. Phys. Earth Planet. Inter. 157(3-4), 181-187.

Liu, X., Zhao, D., 2017. P-wave anisotropy, mantle wedge flow and olivine fabrics beneath Japan. Geophys. J. Int. 210, 1410-1431.

Long, M., 2013. Constraints on subduction geodynamics from seismic anisotropy. Rev. Geophys. 51, 76-112.

Mainprice, D., LePage, Y., Rodgers, J., Jouanna, P., 2007. Predicted elastic properties of the hydrous D phase at mantle pressures: implications for the anisotropy of subducted slabs near 670-km discontinuity and in the lower mantle, Earth Planet. Sci. Lett. 259(3), 283–296.

Marchadier, Y., Rangin, C., 1990. Polyphase tectonics at the southern tip of the Manila trench, Mindoro-Tablas islands, Philippines. Tectonophysics 183, 273-287.

Menant, A., Sternai, P., Jolivet, L., Guillou-Frottier, L., Gerya, T., 2016. 3D numerical modeling of mantle flow, crustal dynamics and magma genesis associated with slab roll-back and tearing: The eastern Mediterranean case. Earth Planet. Sci. Lett. 442, 93-107.

Miyagi, L., Amulele, G., Otsuka, K., Du, Z., Farla, R., Karato, S.I., 2014. Plastic anisotropy and slip systems in ringwoodite deformed to high shear strain in the Rotational Drickamer Apparatus, Phys. Earth Planet. Inter. 228, 244-253.

Nagaya, T., Wallis, S.R., Kobayashi, H., Michibayashi, K., Mizukami, T., Seto, Y., Miyake, A., Matsumoto, M., 2014. Dehydration breakdown of antigorite and the formation of B-type olivine CPO. Earth Planet. Sci. Lett. 387, 67-76.

Nagaya, T., Walker, A.M., Wookey, J., Wallis, S.R., Ishii, K., Kendall, J.M., 2016. Seismic evidence for flow in the hydrated mantle wedge of the Ryukyu subduction zone. Sci. Rep. 6, 29981.

Niu, X., Zhao, D., Li, J., Ruan, A., 2016. P wave azimuthal and radial anisotropy of the Hokkaido subduction zone. J. Geophys. Res. 121, 2636-2660.

Ozawa, A., Tagami, T., Listanco, E.L., Arpa, C.B., Sudo, M., 2004. Initiation and propagation of subduction along the Philippine Trench: Evidence from the temporal and spatial distribution of volcanoes. J. Asian Earth Sci. 23, 105-111.

Paige, C.C., Saunders, M.A., 1982. LSQR: An algorithm for sparse linear equations and sparse least squares. ACM Trans. Math. Softw. 8, 43-71.

Pubellier, M., Quebral, R., Rangin, C., Deffontaines, B., Muller, C., Butterlin, J., 1991. The Mindanao collision zone: A soft collision event within a continuous Neogene strike-slip setting. J. SE Asian Earth Sci. 6, 239-248.

Pubellier, M., Quebral, R., Aurelio, M., Rangin, C., 1996. Docking and post-docking escape tectonics in the southern Philippines. Geo. Soc. London Special Pub., 106, 511-523.

Rangin, C., Le Pichon, X., Mazzotti, S., Pubellier, M., Chamot-Rooke, N., Aurelio, M., Walpersdorf, A., Quebral, R., 1999. Plate convergence measured by GPS across the Sundaland/Philippine Sea plate deformed boundary: The Philippines and eastern Indonesia. Geophys. J. Int. 139, 296-316.

Sasaki, T., Yamazaki, T., Ishizuka, O., 2014. A revised spreading model of the West Philippine Basin. Earth Planets Space 66(1), 1-9.

Smith, W.H.F., Sandwell, D.T., 1997. Global seafloor topography from satellite altimetry and ship depth soundings. Science 277, 1957-1962.

Solomatov, V.S., 2004. Initiation of subduction by small-scale convection. J. Geophys. Res. 109, B01412.

Stern, R.J., Gerya, T., 2017. Subduction initiation in nature and models: A review. Tectonophysics https://doi.org/10.1016/j.tecto.2017.10.014.

Taylor, B., Goodliffe, A.M., 2004. The West Philippine Basin and the initiation of subduction, revisited. Geophys. Res. Lett. 31(12), L12602.

Taylor, B., Hayes, D.E., 1983. Origin and history of the South China Sea basin. In: Hayes, D.E. (Ed.), The Tectonic and Geologic Evolution of Southeast Asian Seas and Islands: Part 2, Geophys. Monogr. Ser. 27. AGU, Washington, DC, pp. 23-56.

Tommasi, A., Mainprice, D., Cordier, P., Thoraval, C., Couvy, H., 2004. Strain-induced seismic anisotropy of wadsleyite polycrystals and flow patterns in the mantle transition zone. J. Geophys. Res. 109, B12405.

Tsujino, N., Nishihara, Y., Yamazaki, D., Seto, Y., Higo, Y., Takahashi, E., 2016. Mantle dynamics inferred from the crystallographic preferred orientation of bridgmanite. Nature 539, 81-84.

Wang, J., Sinogeikin, S.V., Inoue, T., Bass, J.D., 2006. Elastic properties of hydrous ringwoodite at high-pressure conditions. Geophys. Res. Lett. 33, L14308.

Wang, J., Zhao, D., 2008. P-wave anisotropic tomography beneath northeast Japan. Phys. Earth Planet. Inter. 170(1-2), 115-133.

Wang, J., Zhao, D., 2013. P-wave tomography for 3-D radial and azimuthal anisotropy of Tohoku and Kyushu subduction zones. Geophys. J. Int. 193(3), 1166-1181.

Wessel, P., Smith, W., 1998. New, improved version of generic mapping tools released. Eos Trans. AGU 79, 579.

Wright, C., Kuo, B., 2007. Evidence for an elevated 410 km discontinuity below the Luzon, Philippines region and transition zone properties using seismic stations in Taiwan and earthquake sources to the south. Earth Planets Space 59(6), 523-539.

Yumul Jr., G.P., Dimalanta, C.B., Tamayo Jr., R.A., Maury, R.C., 2003. Collision, subduction and accretion events in the Philippines: A synthesis. Island Arc 12, 77-91.

Yumul Jr., G.P., Dimalanta, C.B., Maglambayan, V., Marquez, E.J., 2008. Tectonic setting of a composite terrane: A review of the Philippine island arc system. Geosci. J. 12, 7-17.

Zhang, G.L., Chen, L.H., Jackson, M.G., Hofmann, A.W., 2017. Evolution of carbonated melt to alkali basalt in the South China Sea. Nat. Geosci. 10(3), 229-235.

Zhang, G.L., Luo, Q., Zhao, J., Jackson, M.G., Guo, L.S., Zhong, L.F., 2018. Geochemical nature of sub-ridge mantle and opening dynamics of the South China Sea. Earth Planet. Sci. Lett. 489, 145-155.

Zhao, D., 2015. Multiscale Seismic Tomography, 304 pp., Springer, New York.

Zhao, D., Hasegawa, A., Kanamori, H., 1994. Deep structure of Japan subduction zone as derived from local, regional, and teleseismic events. J. Geophys. Res. 99, 22313-22329.

Zhao, D., Yanada, T., Hasegawa, A., Umino, N., Wei, W., 2012. Imaging the subducting slabs and mantle upwelling under the Japan Islands. Geophys. J. Int. 190, 816-828.

Zhao, D., Yamamoto, Y., Yanada, T., 2013. Global mantle heterogeneity and its influence on teleseismic regional tomography. Gondwana Res. 23, 595-616.

Zhao, D., Yu, S., Liu, X., 2016. Seismic anisotropy tomography: New insight into subduction dynamics. Gondwana Res. 33, 24-43.

Physics of the Earth and Planetary Interiors

Supporting Information for

P-wave anisotropic tomography of the central and southern Philippines

Jianke Fan[a, b], Dapeng Zhao[b]

a CAS Key Laboratory of Marine Geology and Environment, Institute of Oceanology, Chinese Academy of Sciences, Qingdao 266071, China. E-mail: fanjianke@qdio.ac.cn

b Department of Geophysics, Graduate School of Science, Tohoku University, Sendai 980-8578, Japan

Contents of this file

Figs. S1 to S30.

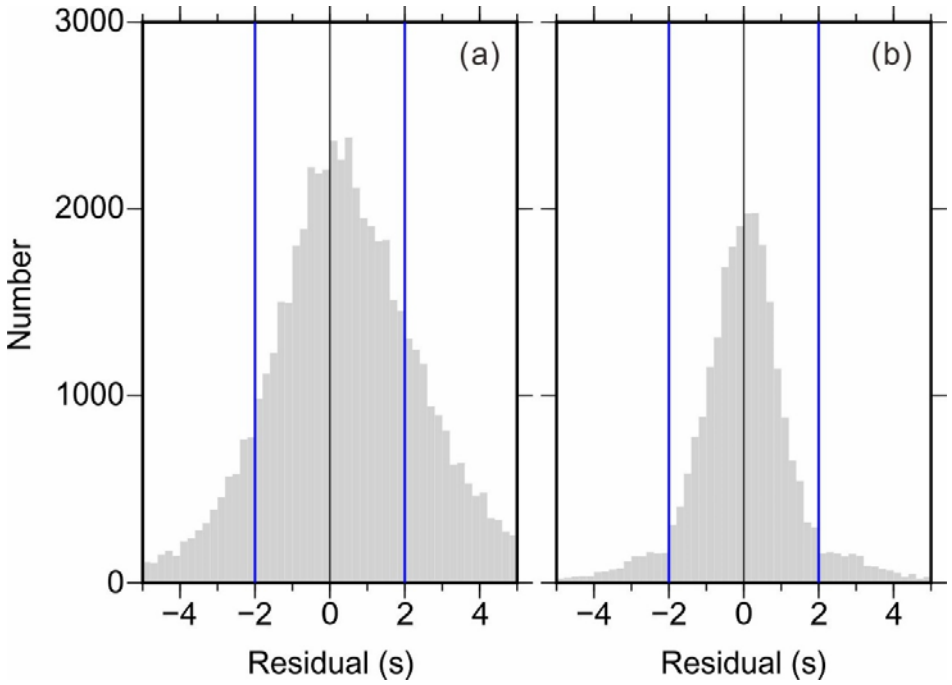

Fig. S1. Histograms of (a) local-earthquake travel-time residuals and (b) teleseismic relative travel-time residuals. The blue lines denote the cutoff residuals adopted for tomographic inversions in this study.

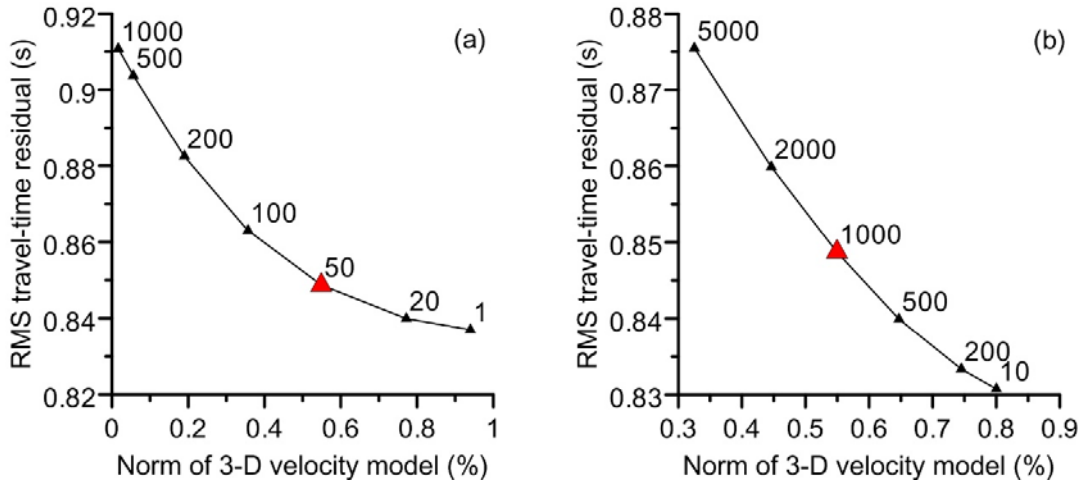

Fig. S2. Trade-off curves between the norm of the 3-D velocity model and the RMS travel-time residual for Vp isotropic tomography, with different values (the numbers beside the triangles) of the damping parameter (a) and the smoothing parameter (b). The larger red triangles denote the optimal values of the damping and smoothing parameters.

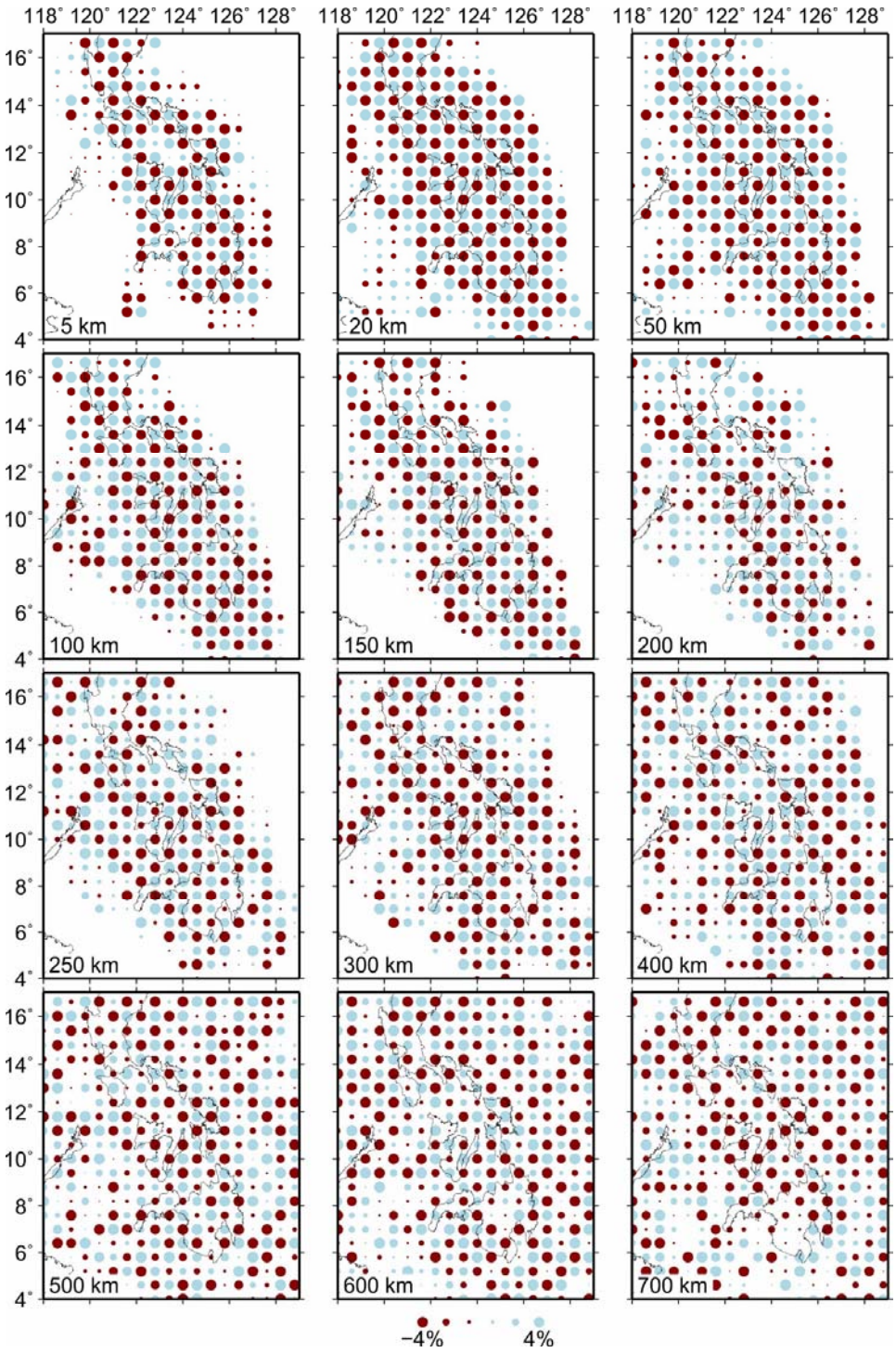

Fig. S3. Results of a checkerboard resolution test (CRT) with a lateral grid interval of 0.6°. The layer depth is shown at the lower-left corner of each map. The red and blue dots denote low and high Vp perturbations, respectively, whose scale is shown at the bottom.

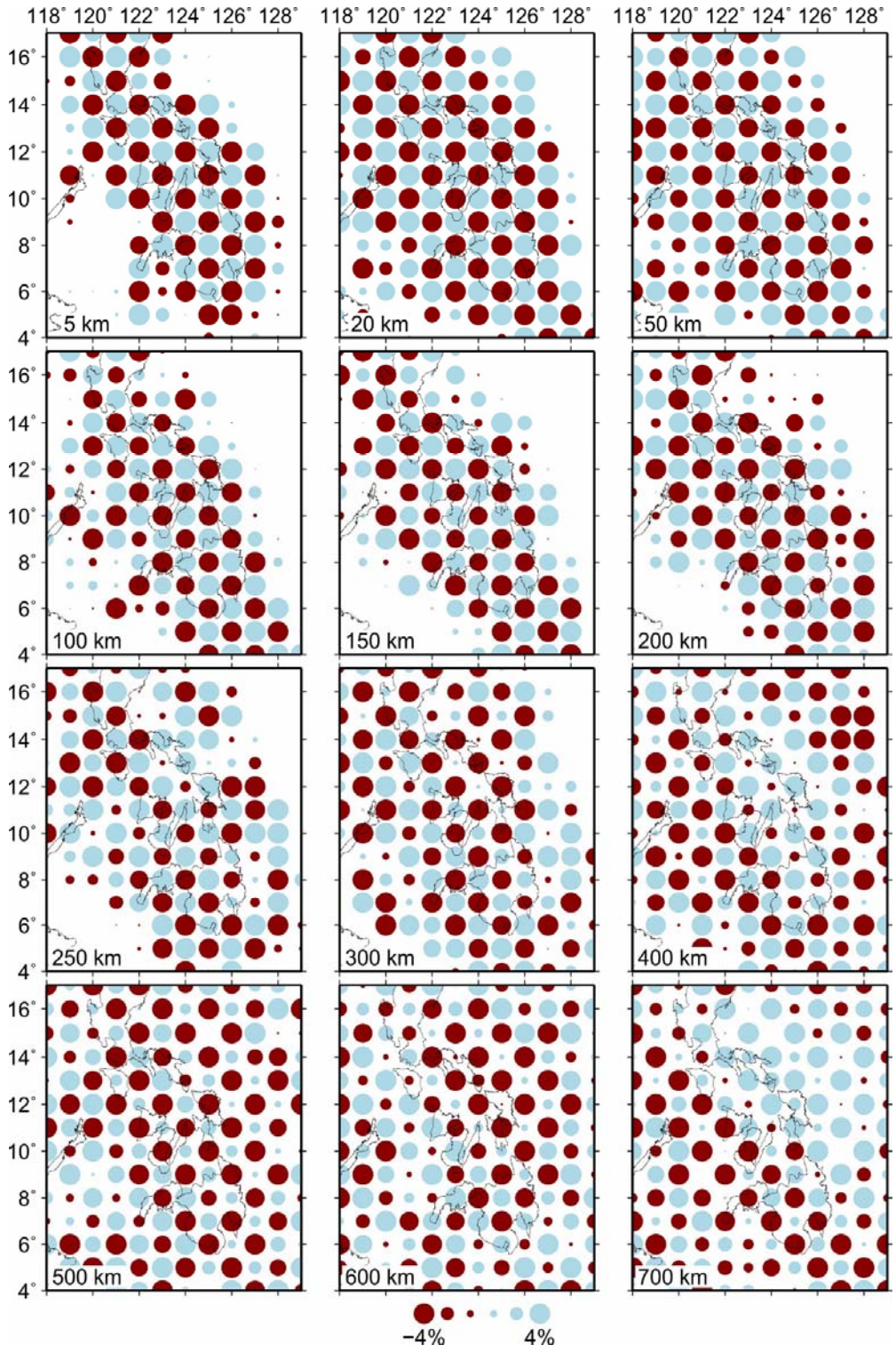

Fig. S4. The same as Fig. S3 but the lateral grid interval is 1.0°.

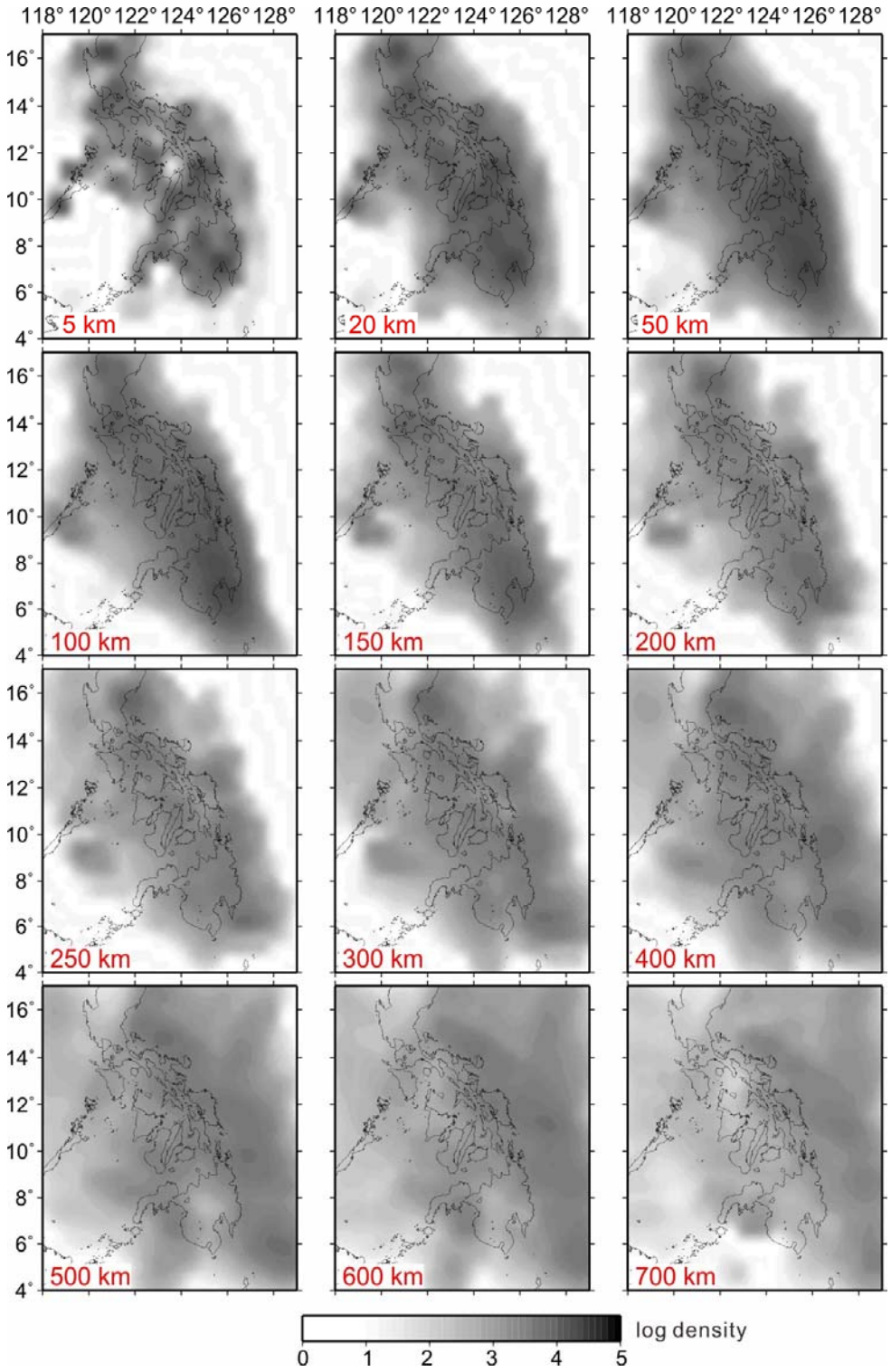

Fig. S5. Ray density distribution in a logarithmic scale as shown at the bottom. The layer depth is shown at the lower-left corner of each map.

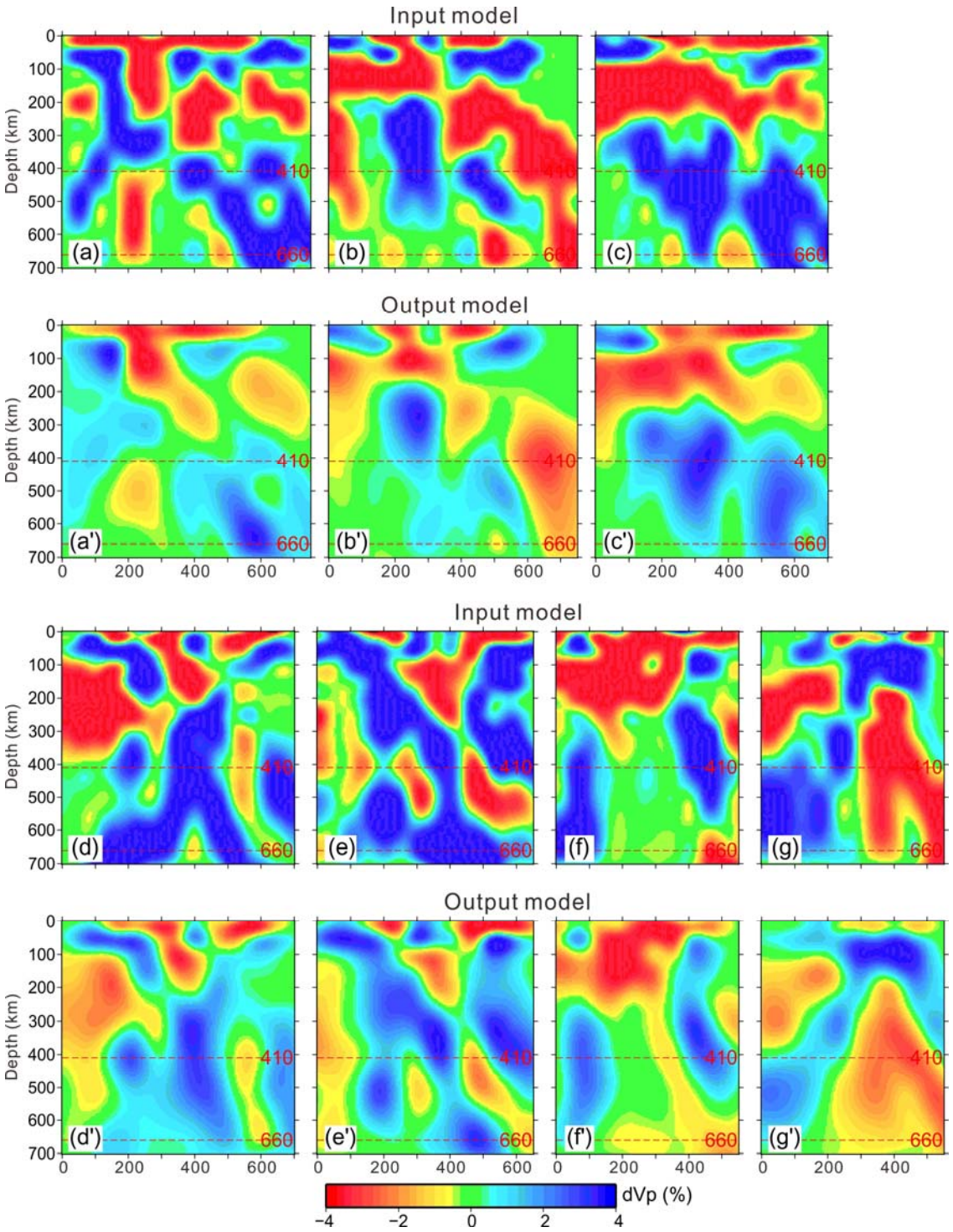

Fig. S6. Results of a restoring resolution test (RRT) for isotropic Vp tomography (see text for details). The two horizontal dashed lines denote the 410 and 660 km discontinuities. The Vp perturbation scale is shown at the bottom.

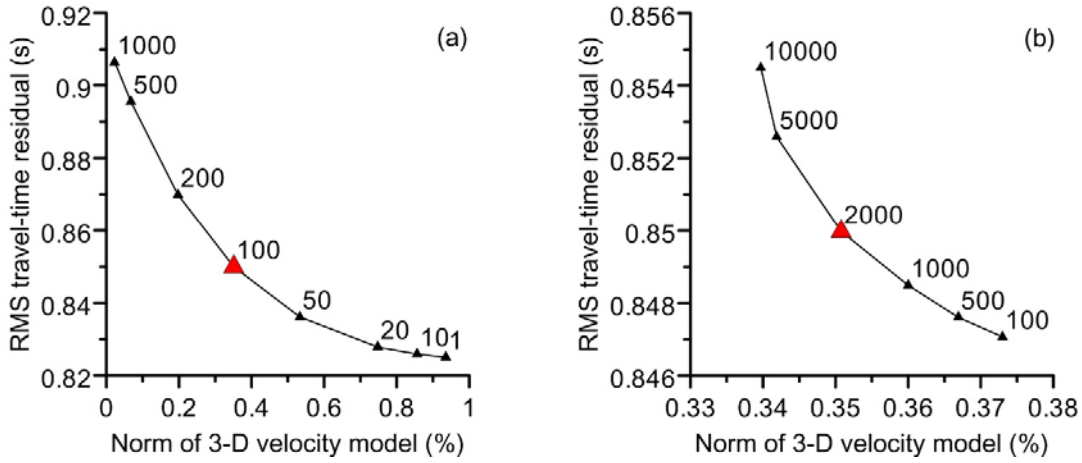

Fig. S7. The same as Fig. S2 but for Vp azimuthal anisotropy tomography.

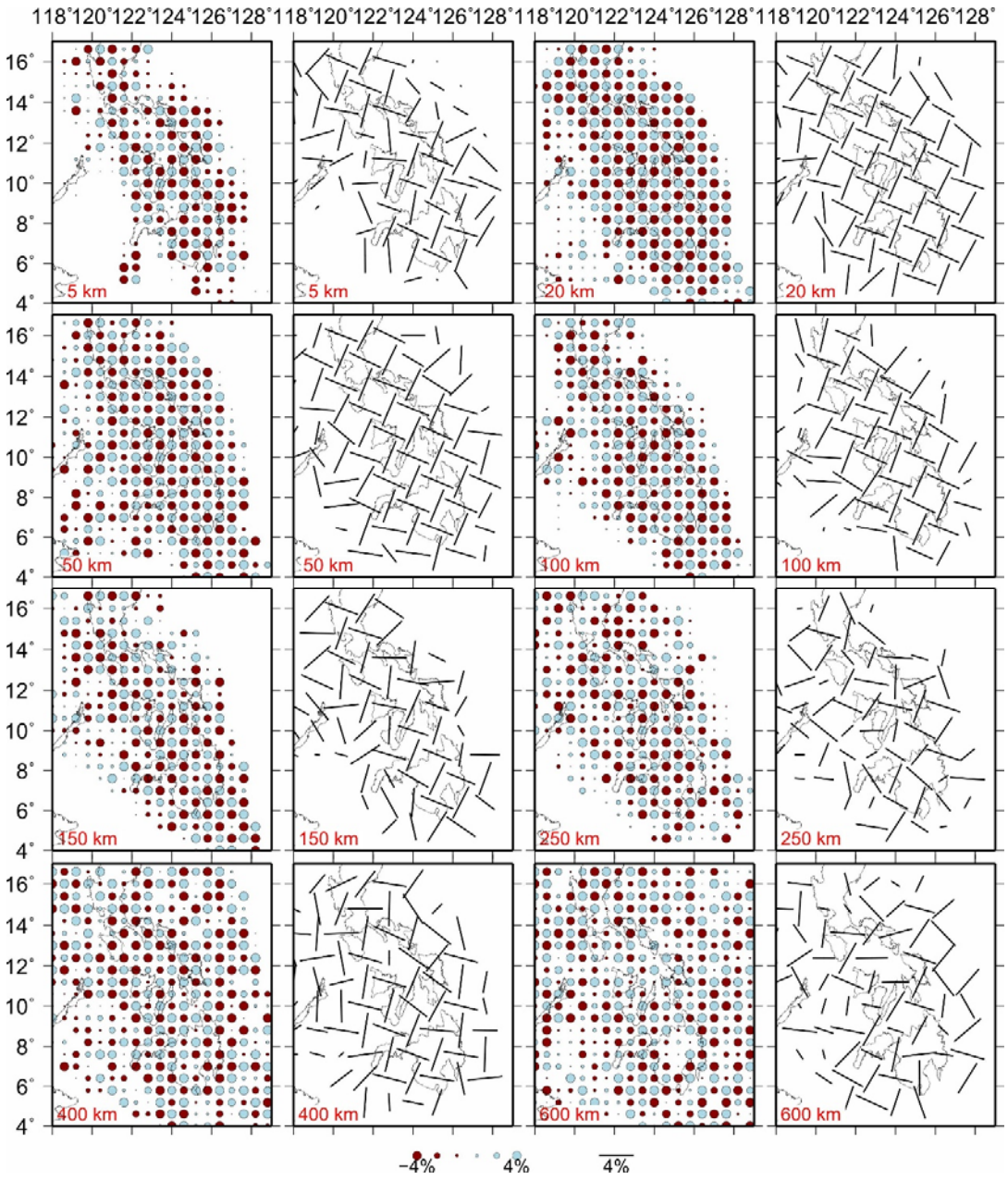

Fig. S8. Results of a CRT for Vp azimuthal anisotropy tomography with isotropic Vp perturbations of ±4% and azimuthal anisotropic (A and B) perturbations of ±3% in the input model. The lateral grid interval is 0.6° for the isotropic Vp and 1.2° for the azimuthal anisotropy. The red and blue dots denote low and high isotropic Vp perturbations, respectively. The orientation and length of the black bars denote the fast velocity directions (FVDs) and the amplitude, respectively, of Vp azimuthal anisotropy. The layer depth is shown at the lower-left corner of each map. The scales of the isotropic Vp and anisotropic amplitude are shown at the bottom.

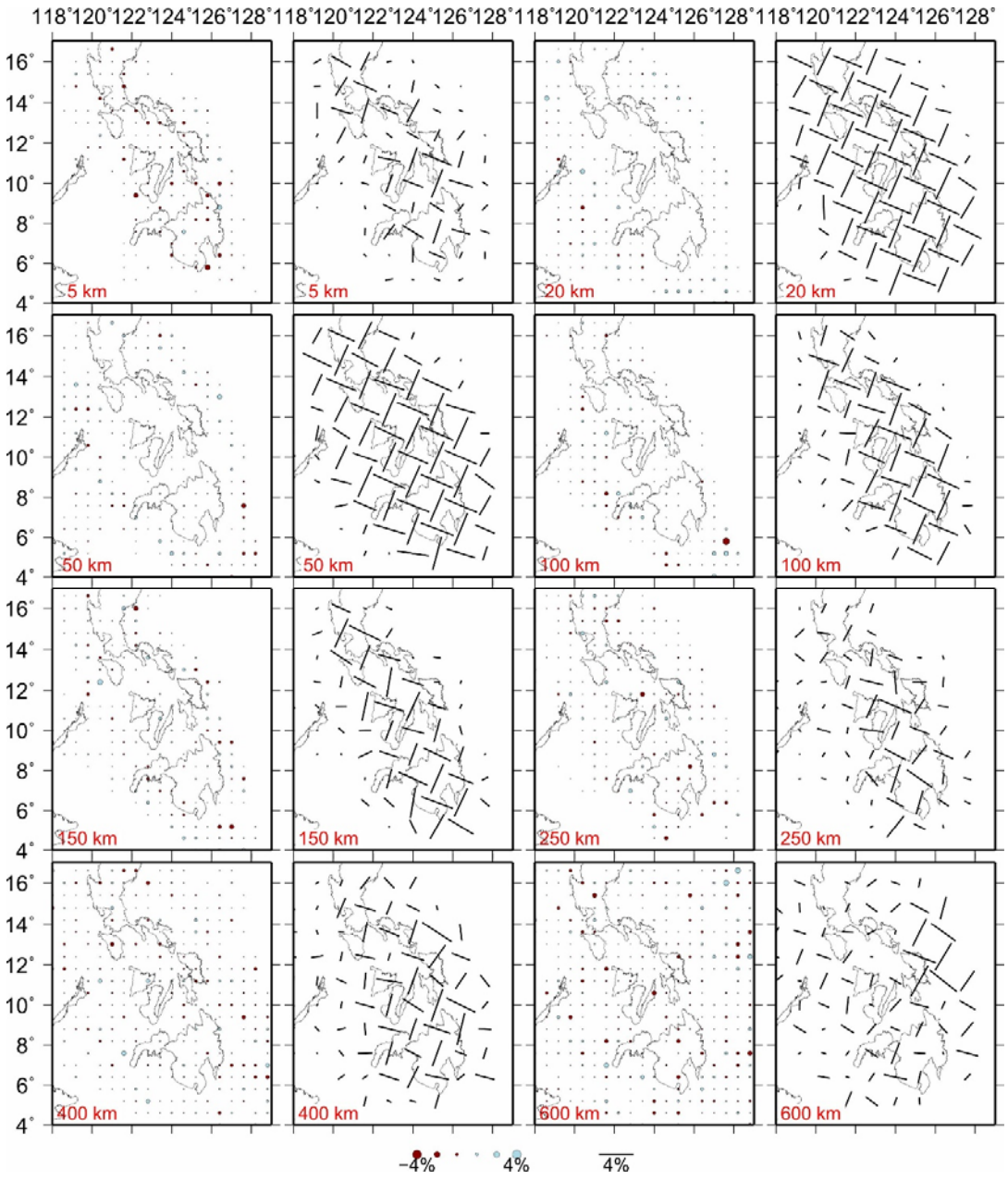

Fig. S9. The same as Fig. S8 but in the input model the azimuthal anisotropy (A and B) perturbations are ±3% and the isotropic Vp perturbation is 0.

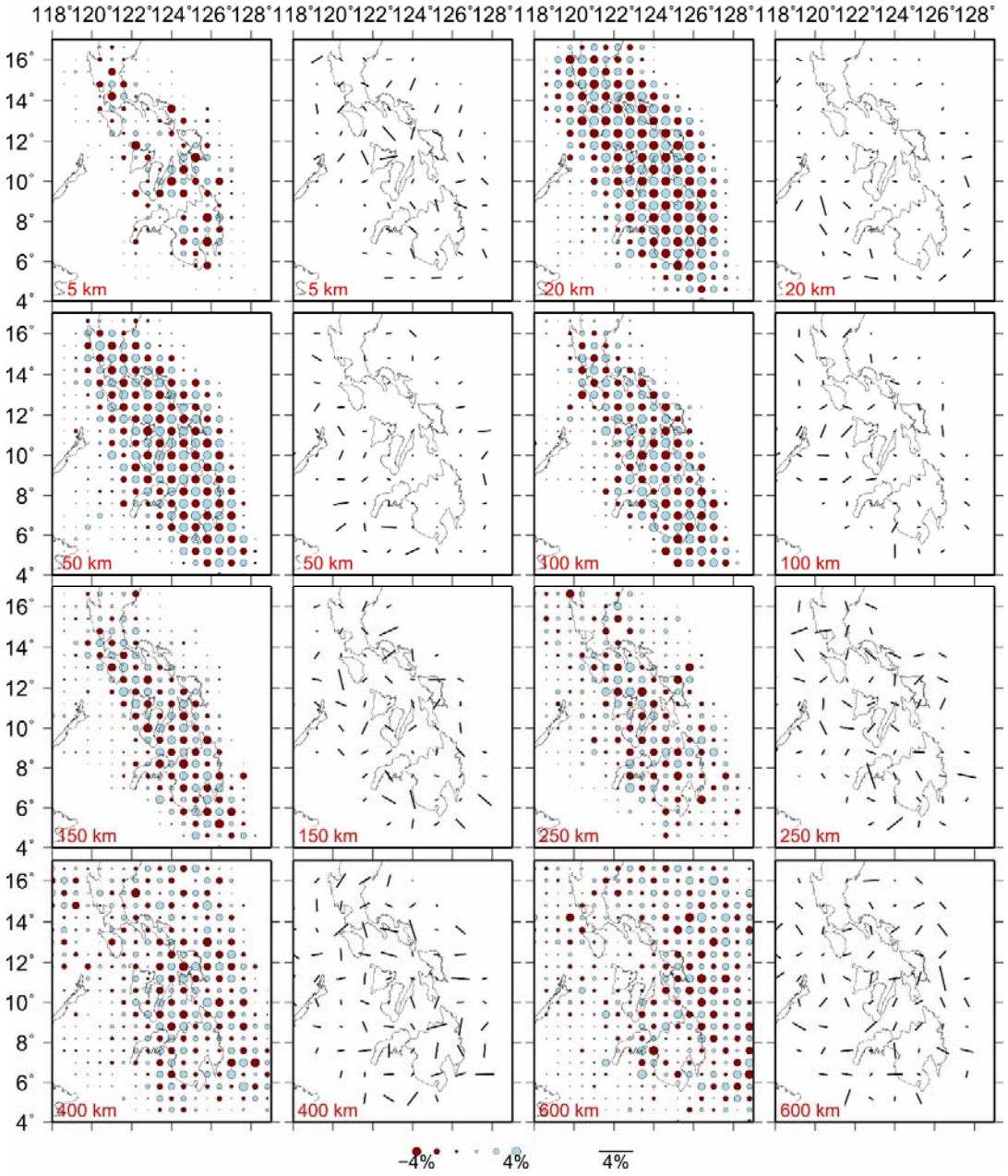

Fig. S10. The same as Fig. S8 but in the input model the isotropic Vp perturbations are ±4% and the azimuthal anisotropy perturbation is 0.

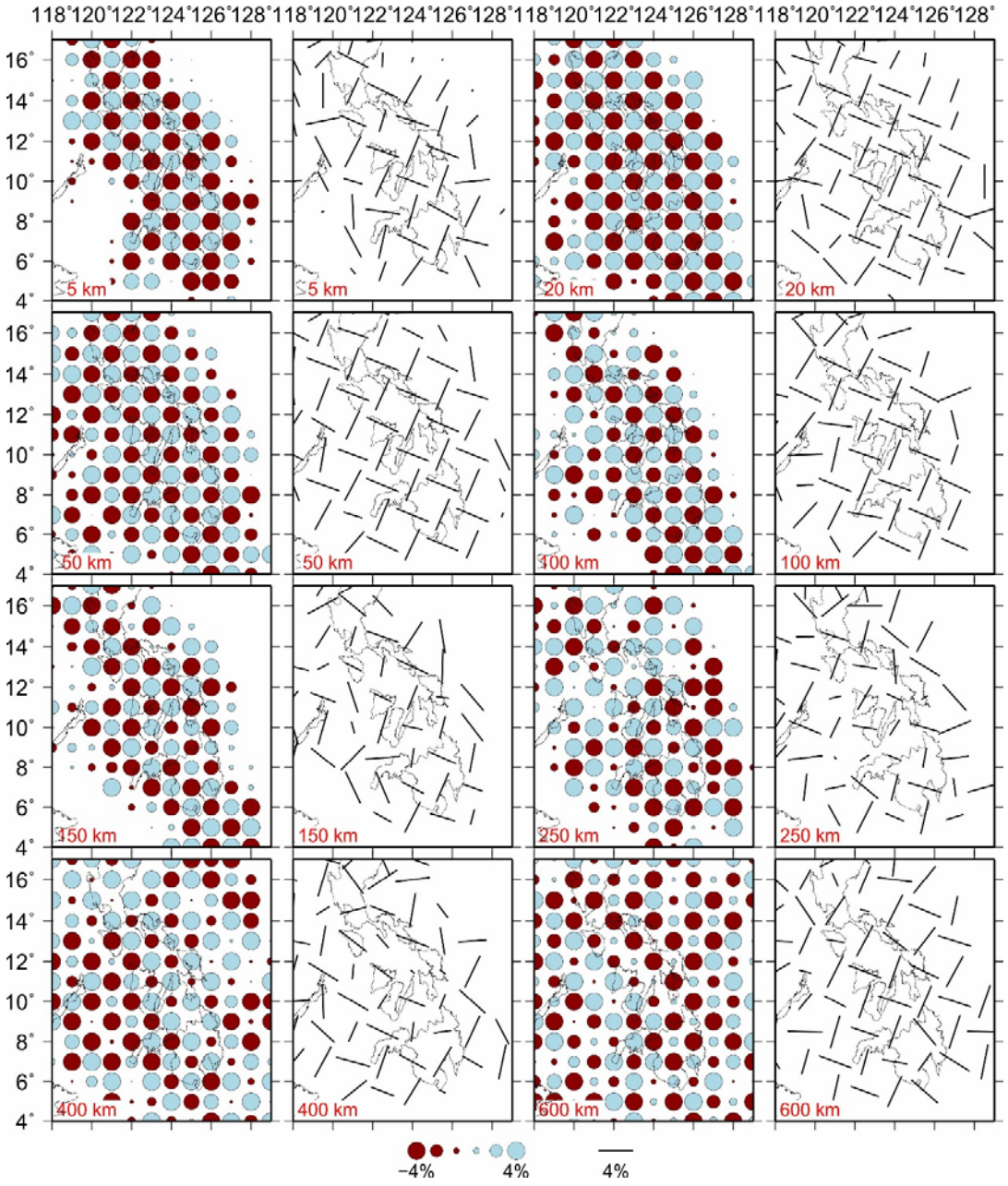

Fig. S11. The same as Fig. S8 but the lateral grid interval is 1.0° for the isotropic Vp and 1.5° for the azimuthal anisotropy.

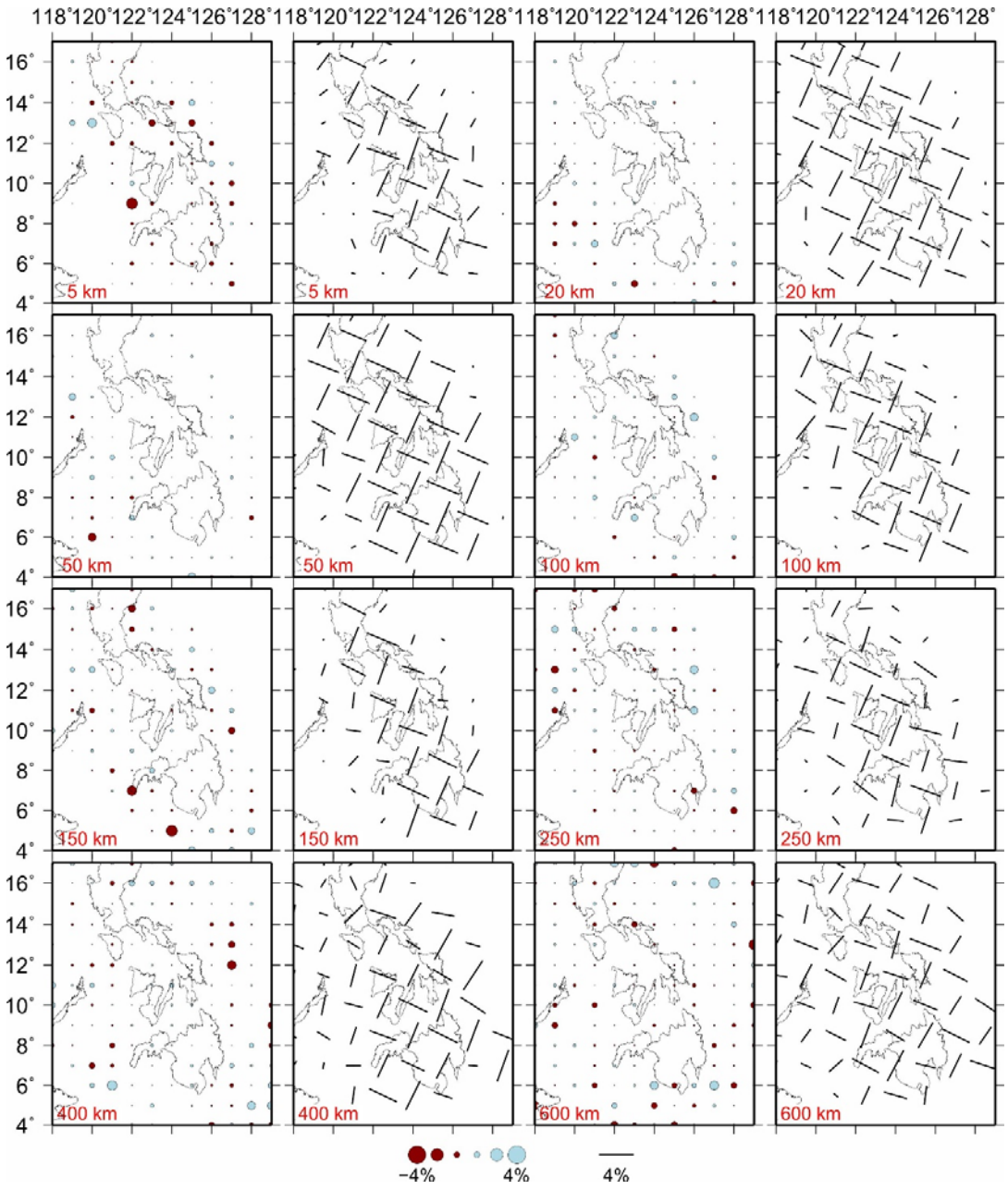

Fig. S12. The same as Fig. S11 but in the input model the azimuthal anisotropy (A and B) perturbations are ±3% and the isotropic Vp perturbation is 0.

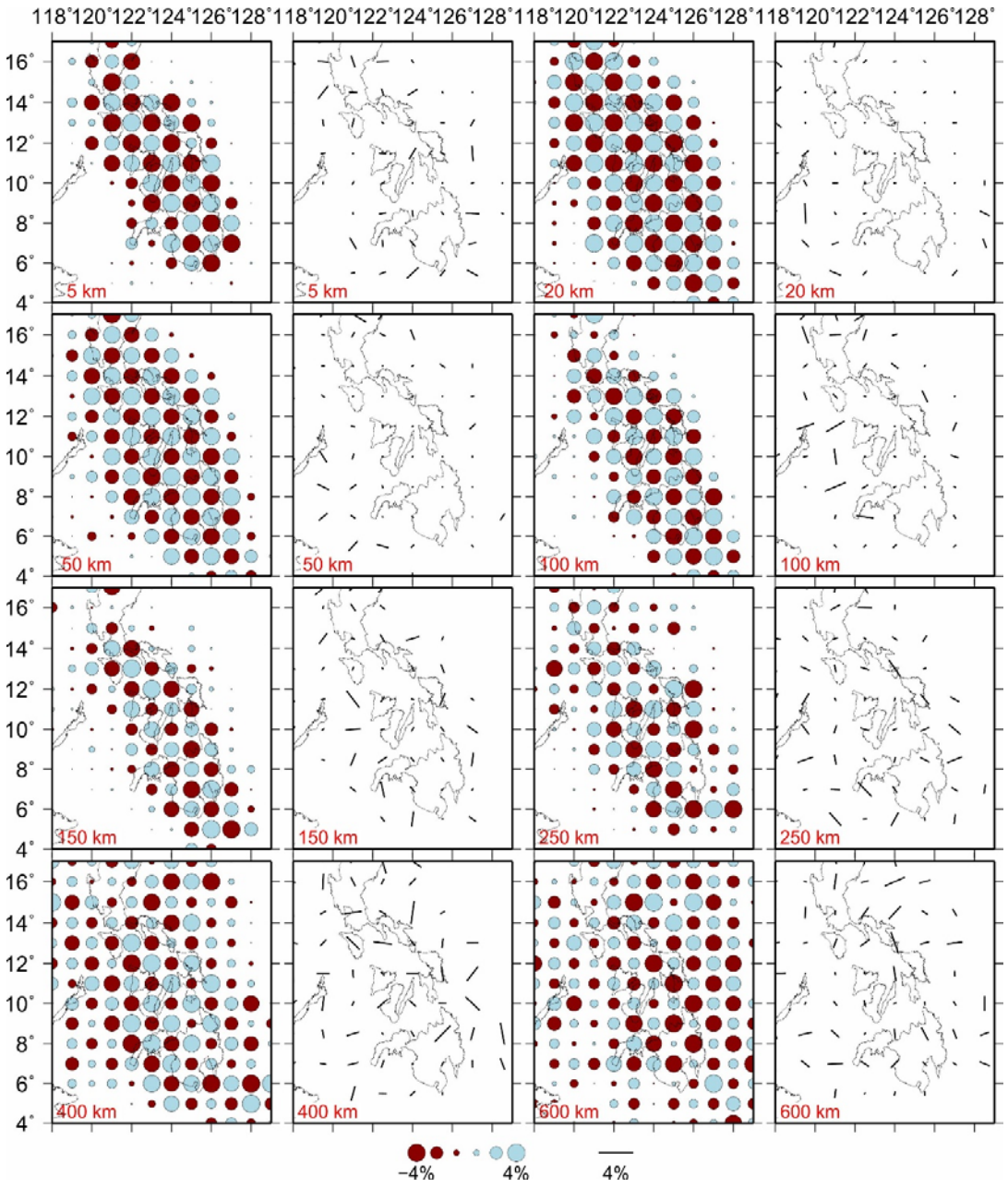

Fig. S13. The same as Fig. S11 but in the input model the isotropic Vp perturbations are ±4% and the azimuthal anisotropy perturbation is 0.

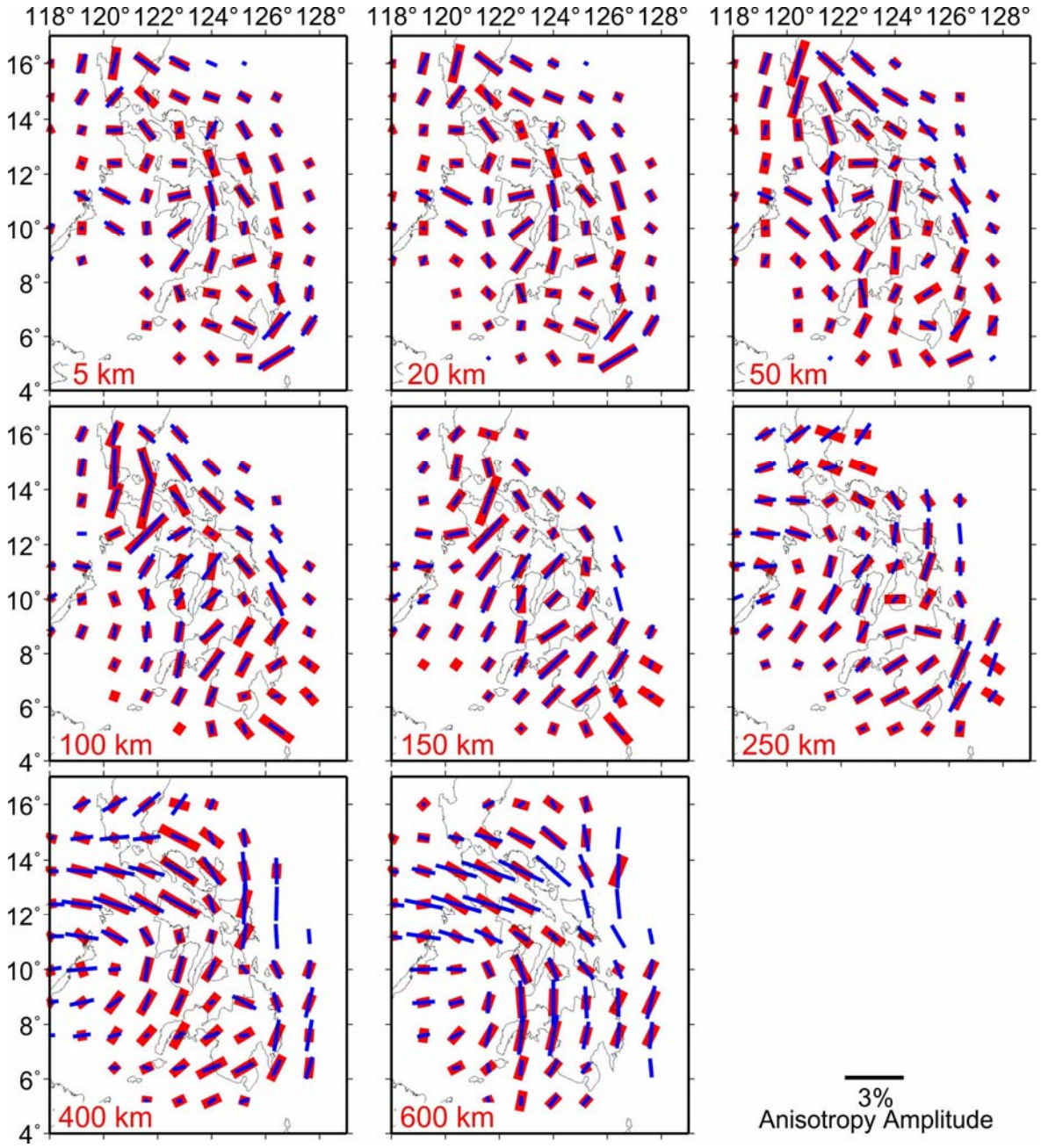

Fig. S14. Azimuthal anisotropy results of a RRT for Vp azimuthal anisotropy tomography. The obtained results (Fig. 5) are taken to be the input model. Gaussian random noise with a standard deviation of 0.1 s is added to the theoretical travel times before the inversion. The red bars denote the input model of anisotropy, whereas the blue bars represent the anisotropic results of the RRT. The orientation and length of the bars denote the FVDs and amplitude of the azimuthal anisotropy, respectively, whose scale is shown at the bottom.

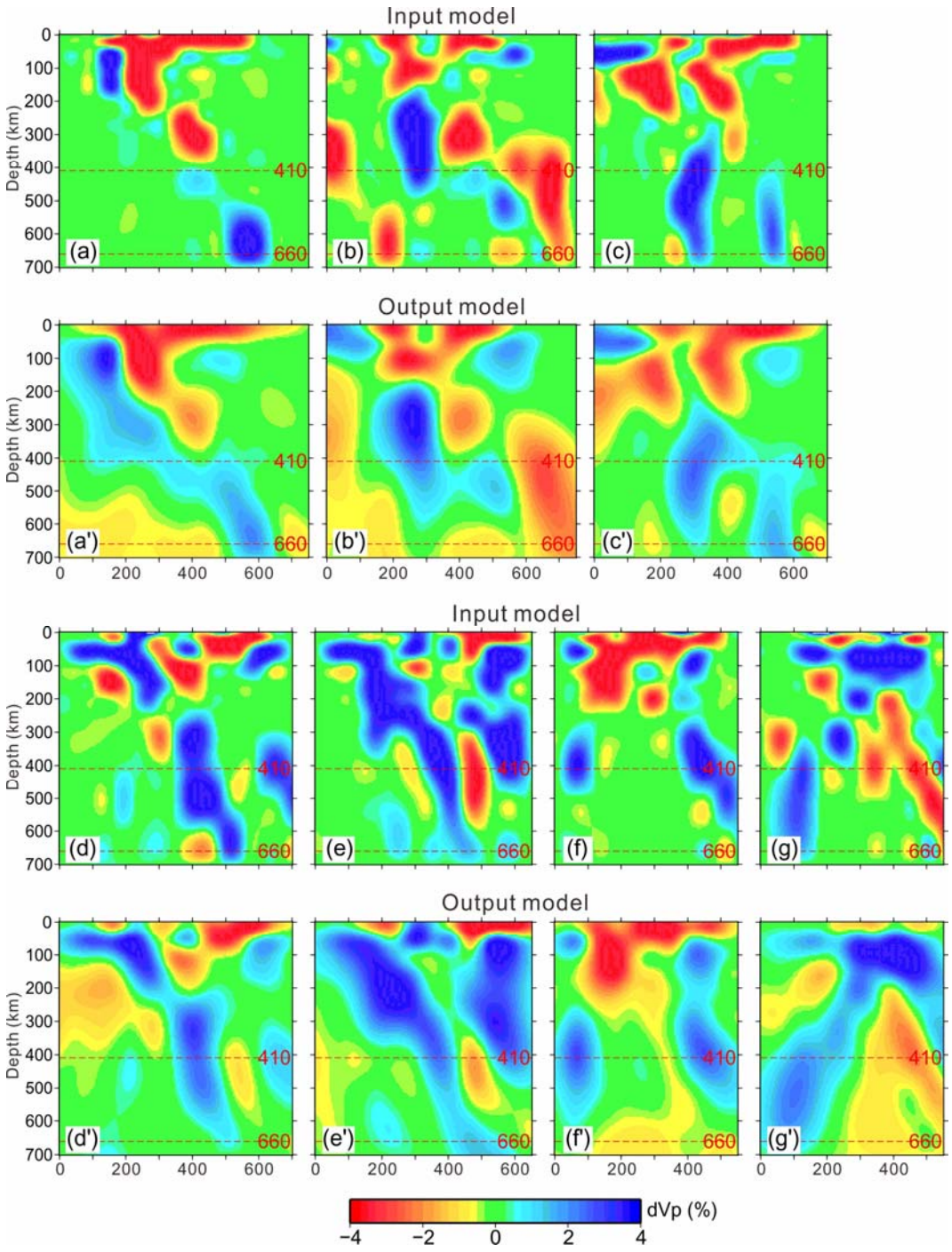

Fig. S15. The same as Fig. S14 but for the vertical cross-sections of isotropic Vp image. The obtained isotropic part of the azimuthal anisotropy tomography (Fig. 5) is taken to be the input model, which is shown in the upper panels. The lower panels show the isotropic results of the RRT. The red and blue colors denote low and high Vp perturbations, respectively, whose scale is shown at the bottom.

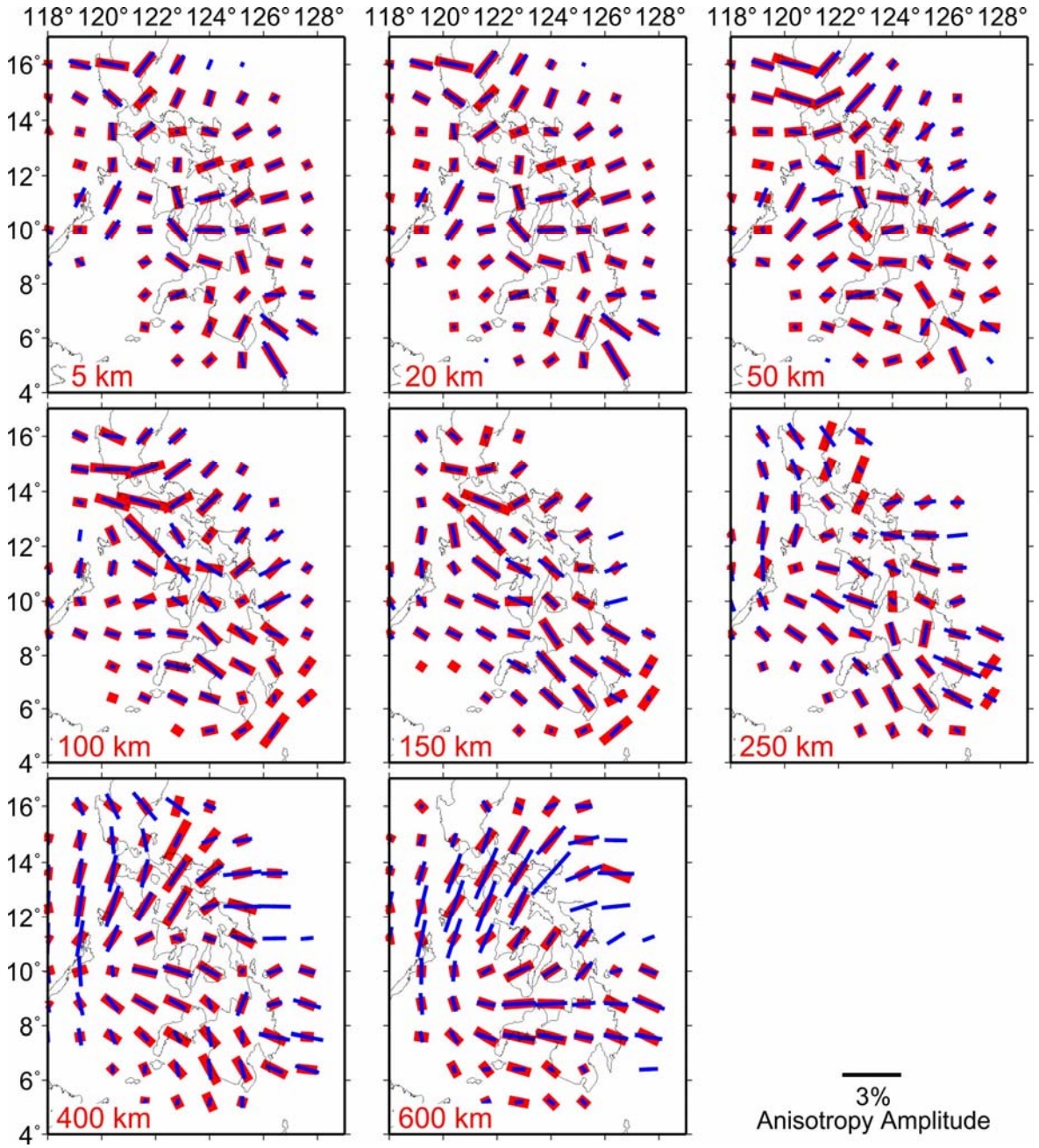

Fig. S16. The same as Fig. S14, but patterns of the obtained azimuthal anisotropy and the isotropic Vp (Fig. 5) are reversed and then taken to be the input model. Gaussian random noise with a standard deviation of 0.1 s is added to the theoretical travel times before the inversion. The red bars denote the input model of anisotropy, whereas the blue bars represent the anisotropic results of the RRT. The orientation and length of the bars denote the FVDs and amplitude of the azimuthal anisotropy, respectively, whose scale is shown at the bottom.

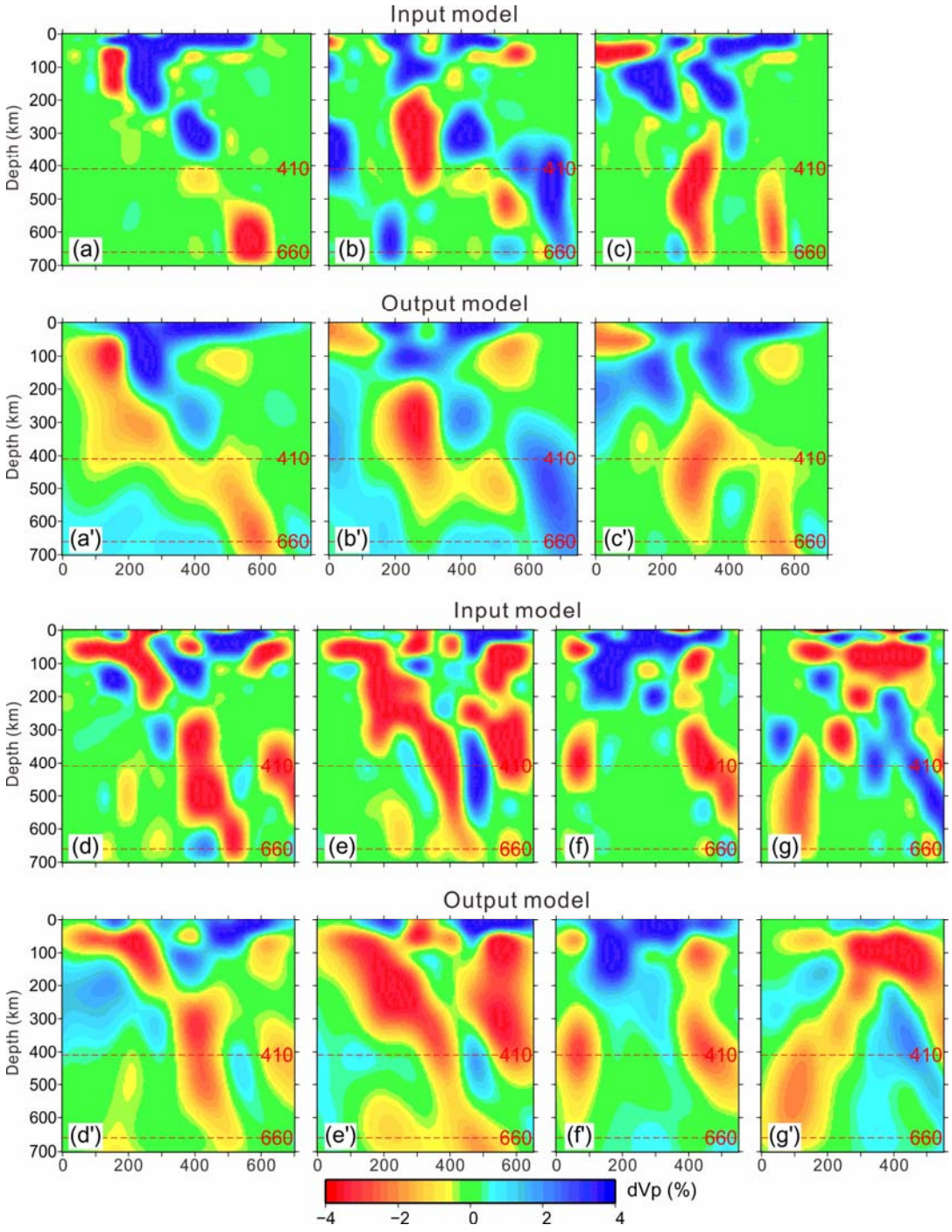

Fig. S17. The same as Fig. S16 but for the vertical cross-sections of isotropic velocity. The obtained isotropic part of the azimuthal anisotropy tomography (Fig. 5) is taken to be the input model, which is shown in the upper panels. The lower panels show the isotropic results of the RRT. The red and blue colors denote low and high Vp perturbations, respectively, whose scale is shown at the bottom.

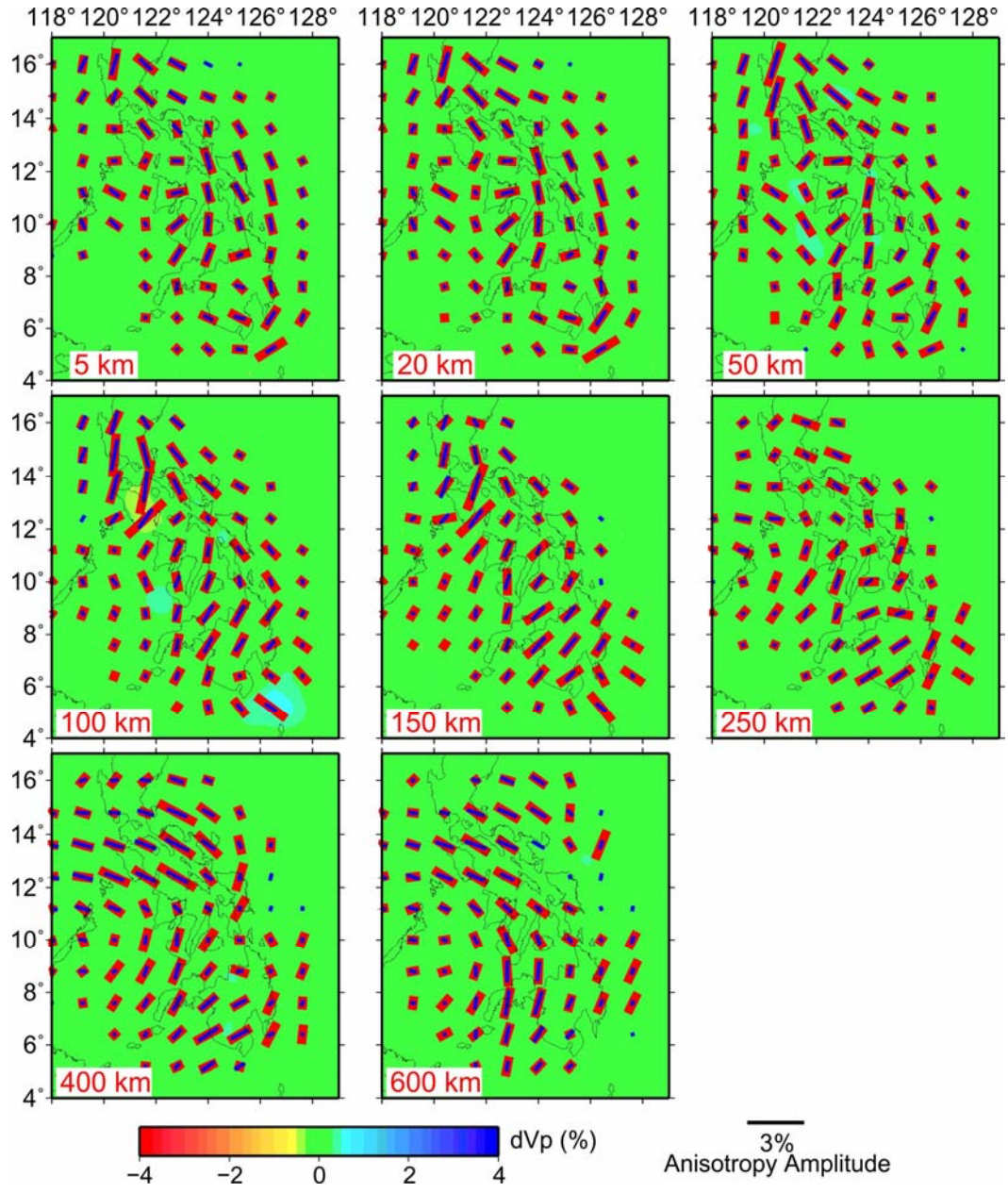

Fig. S18. Results of a RRT for Vp azimuthal anisotropy tomography. The obtained results of azimuthal anisotropy (Fig. 5) are taken to be the input model but isotropic Vp anomalies are assumed to be zero. Gaussian random noise with a standard deviation of 0.1 s is added to the theoretical travel times before the tomographic inversion. The red bars show the input model of azimuthal anisotropy, and the blue bars represent the anisotropic results of the test. The red and blue colors denote low and high isotropic Vp perturbations, respectively. The scales of the isotropic velocity and the azimuthal anisotropy are both shown at the bottom.

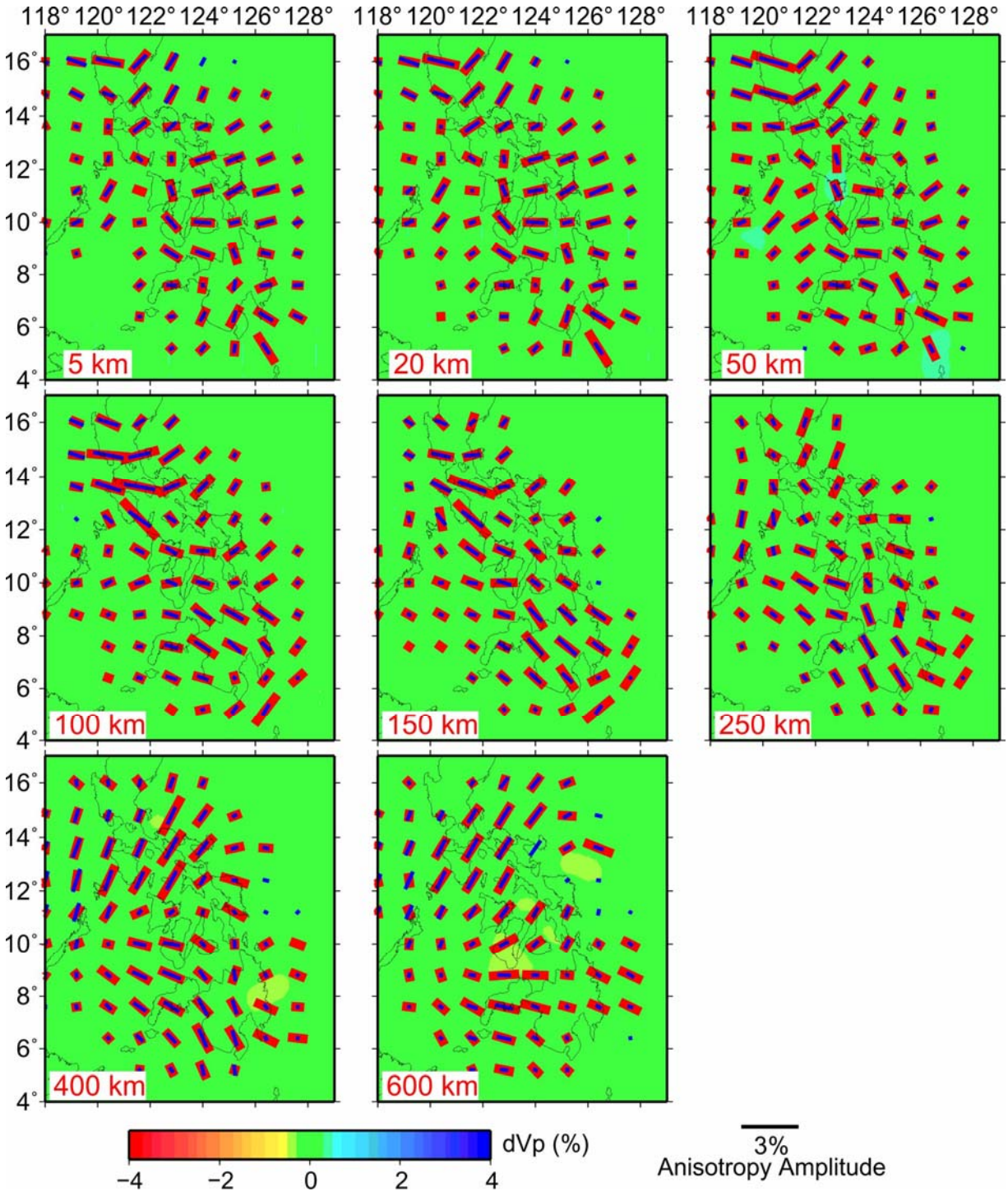

Fig. S19. Results of a synthetic test for Vp azimuthal anisotropic tomography. The obtained FVDs of azimuthal anisotropy (Fig. 5) are rotated by 90 degrees and then taken to be the input model but isotropic Vp anomalies are assumed to be zero.

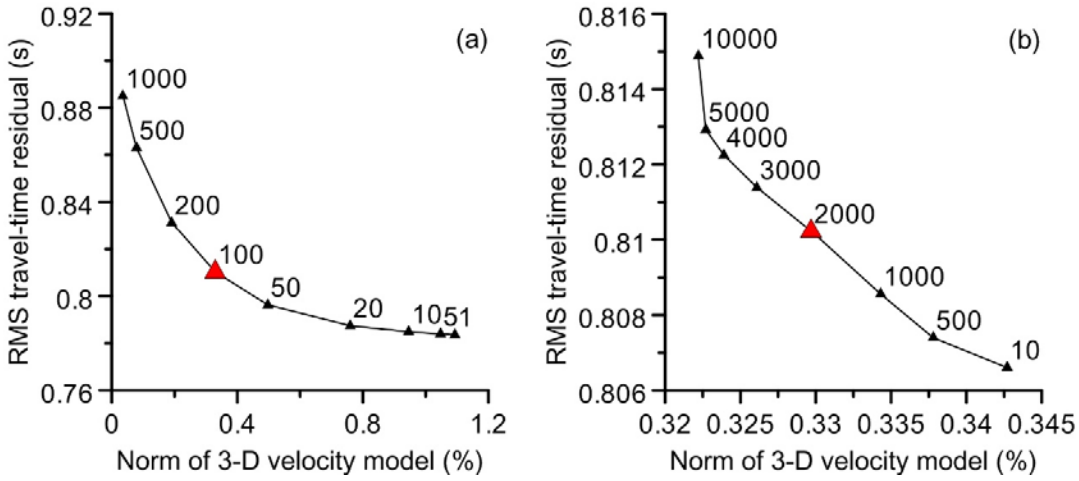

Fig. S20. The same as Fig. S2 but for P-wave radial anisotropy tomography.

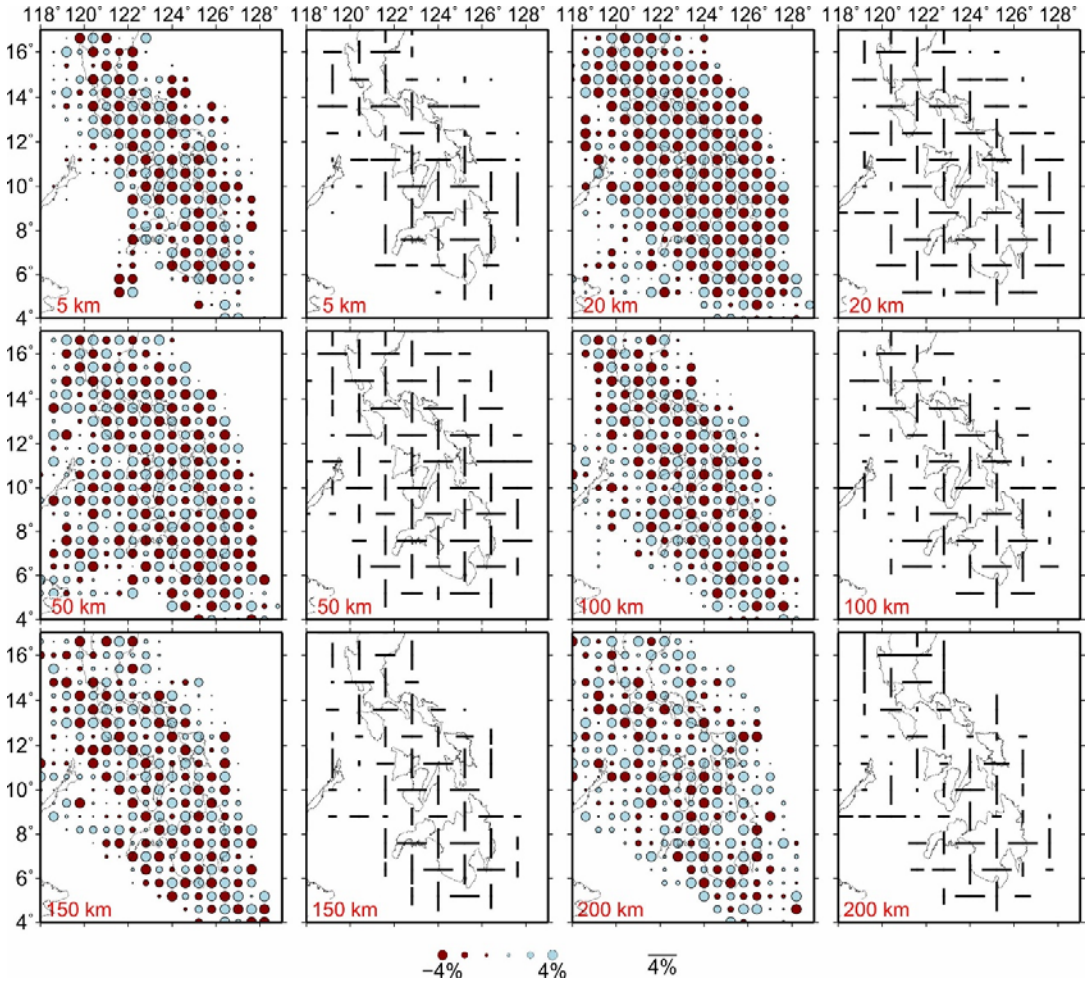

Fig. S21. Results of a CRT for P-wave radial anisotropy tomography with the isotropic Vp perturbations of ±4% and the radial anisotropic perturbations of ±4%. The lateral grid interval is 0.6° for the isotropic Vp and 1.2° for the radial anisotropy. The red and blue dots denote low and high Vp perturbations, respectively. The horizontal and vertical bars represent positive (i.e., $\boldsymbol{V_{ph} > V_{pv}}$) and negative (i.e., $\boldsymbol{V_{ph} < V_{pv}}$) radial anisotropies, respectively, whose lengths denote the amplitude of anisotropy. The layer depth is shown at the lower-left corner of each map. The scales of the isotropic Vp and radial anisotropy are shown at the bottom.

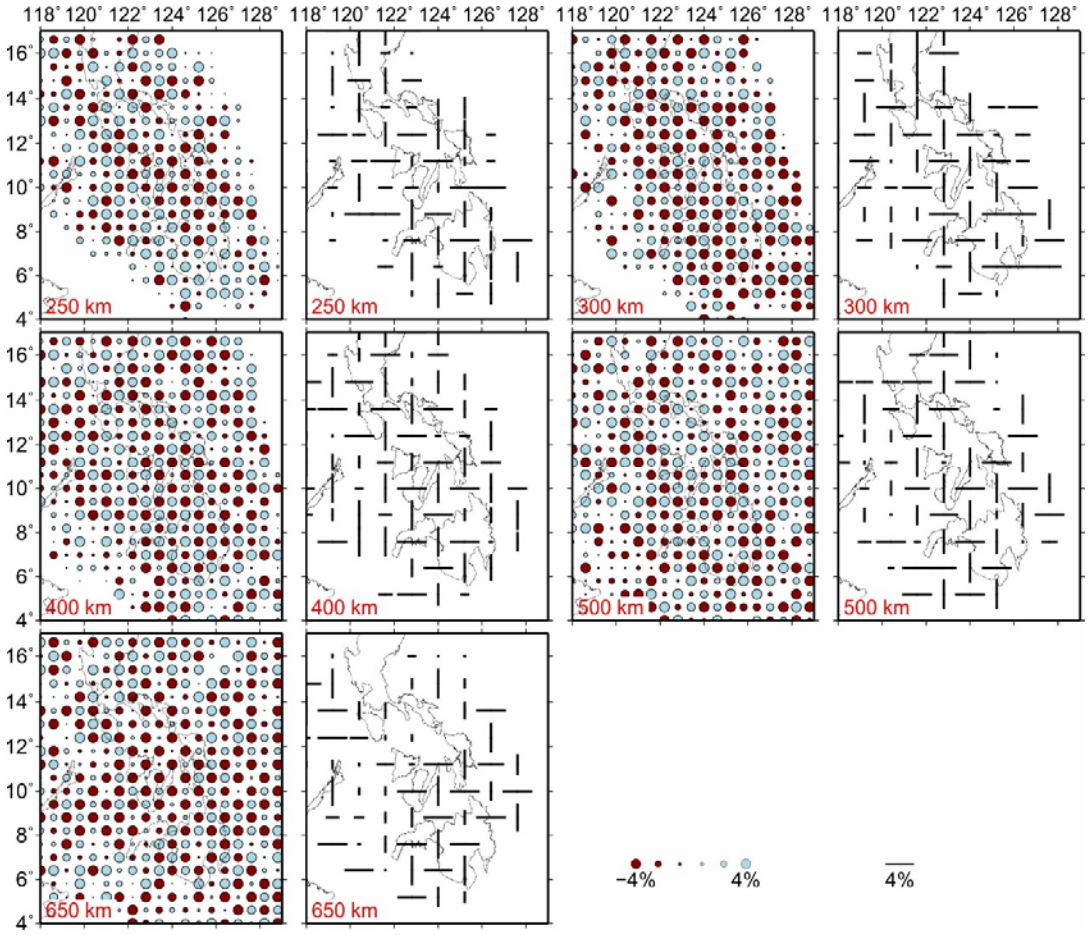

Fig. S21. (continued)

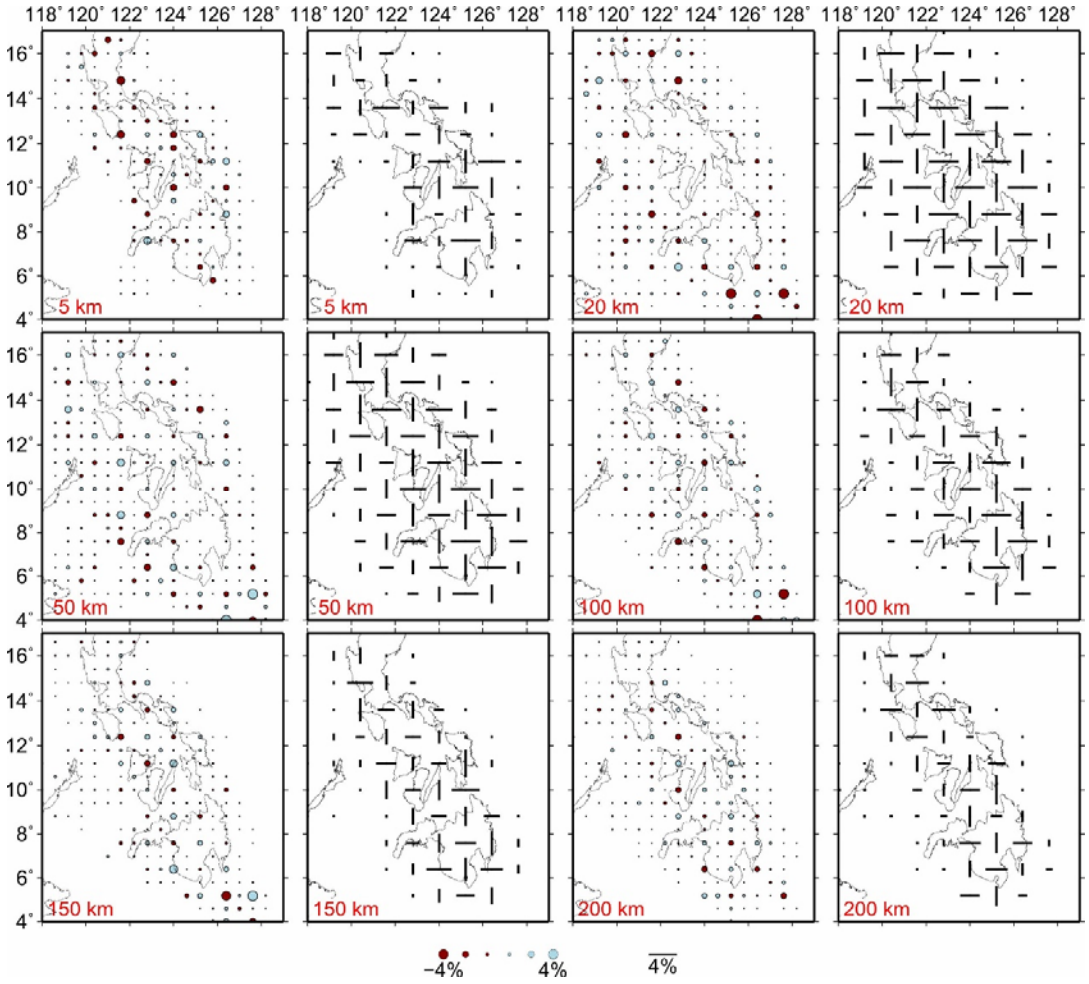

Fig. S22. The same as Fig. S21 but in the input model the radial anisotropic perturbations are ±4% and the isotropic Vp perturbation is 0.

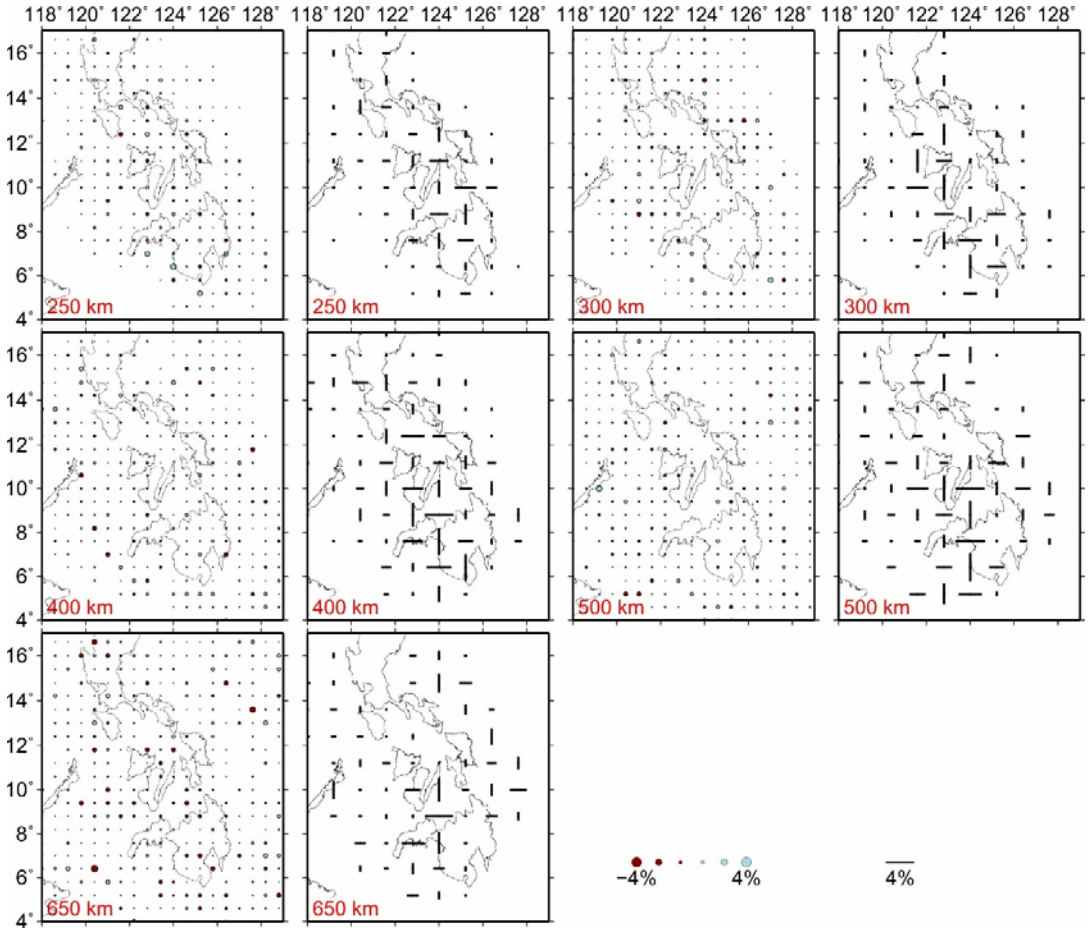

Fig. S22. (continued)

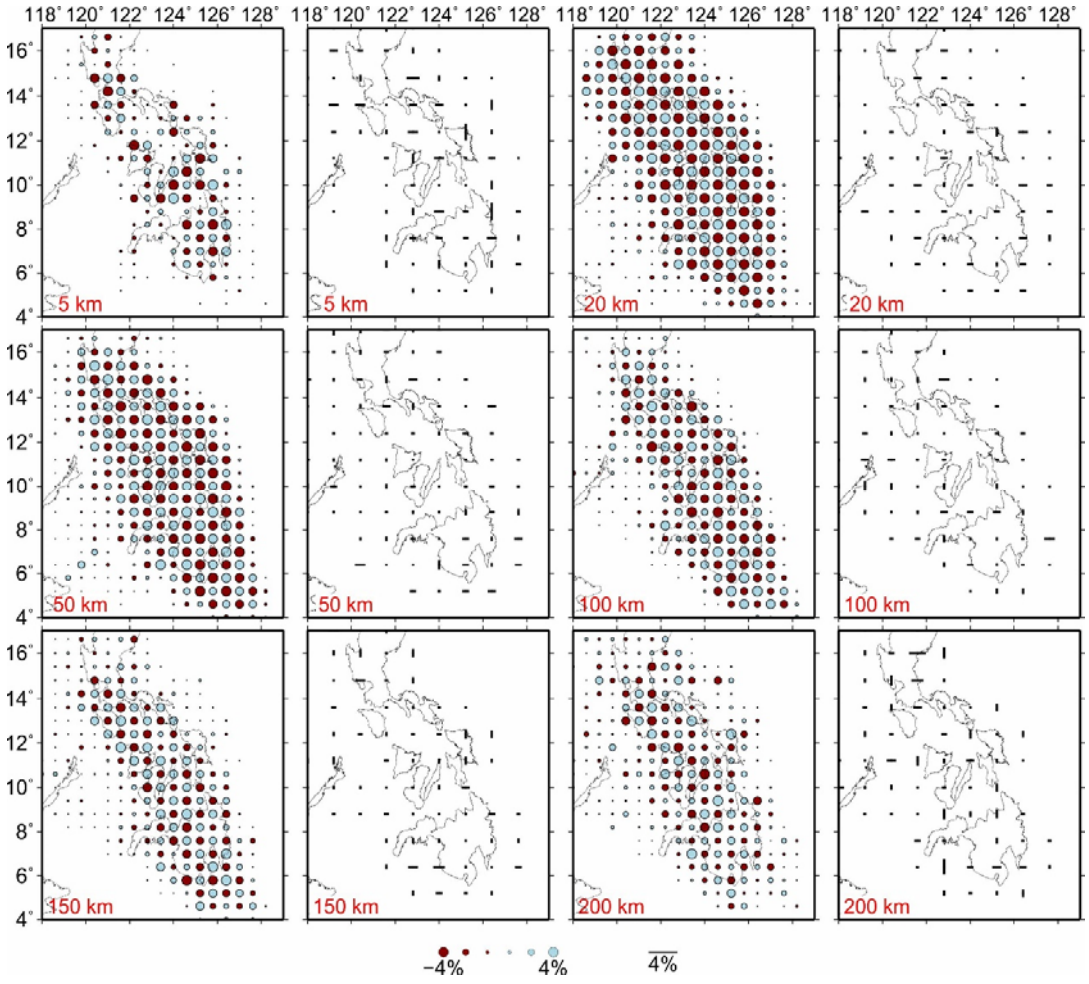

Fig. S23. The same as Fig. S21 but in the input model the isotropic Vp perturbations are ±4% and the radial anisotropic perturbation is 0.

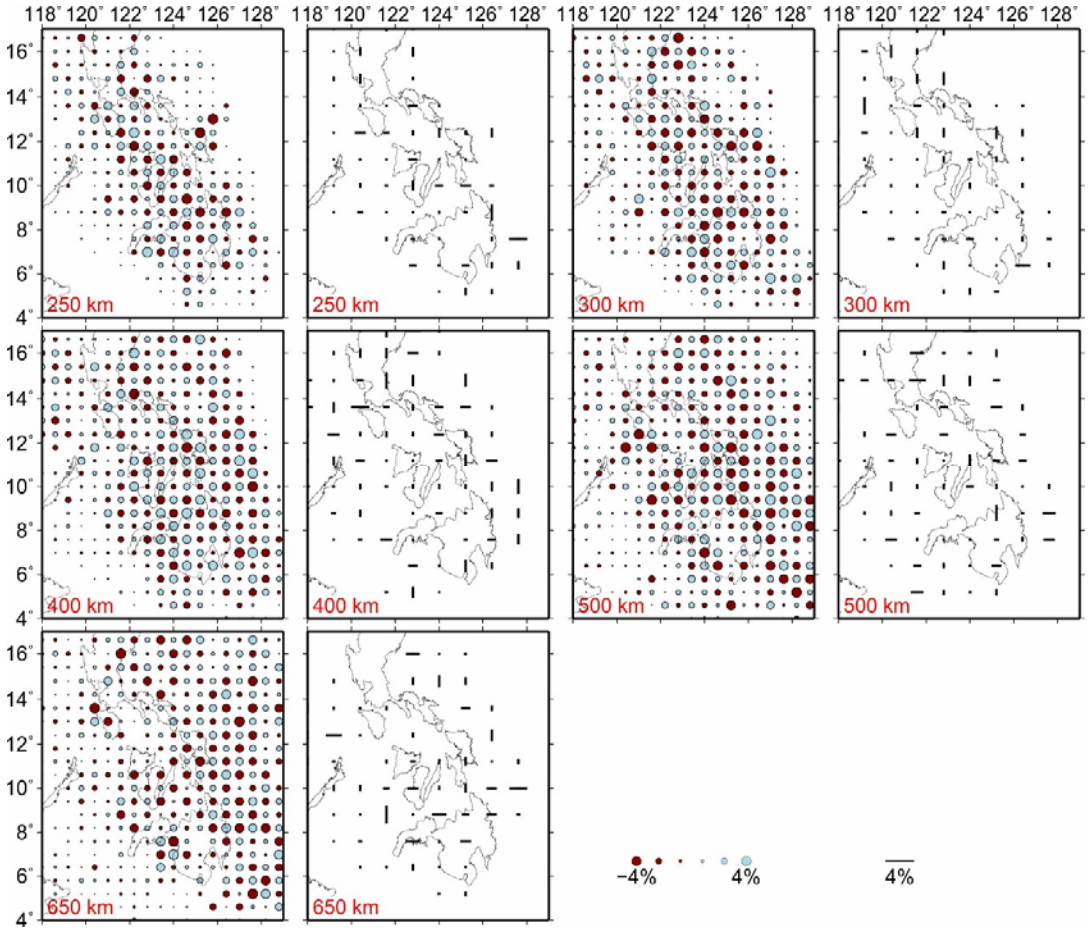

Fig. S23. (continued)

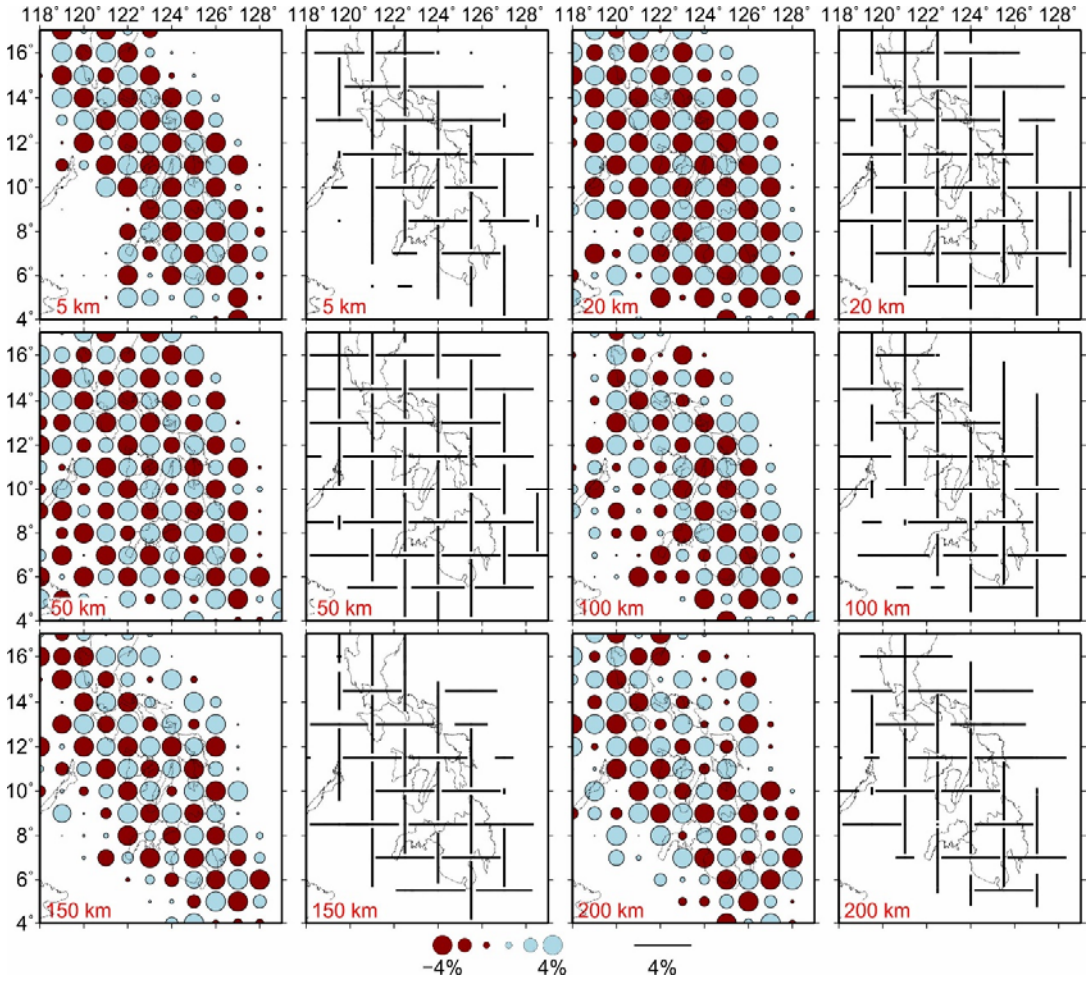

Fig. S24. The same as Fig. S21 but the lateral grid interval is 1.0° for the isotropic Vp and 1.5° for the radial anisotropy.

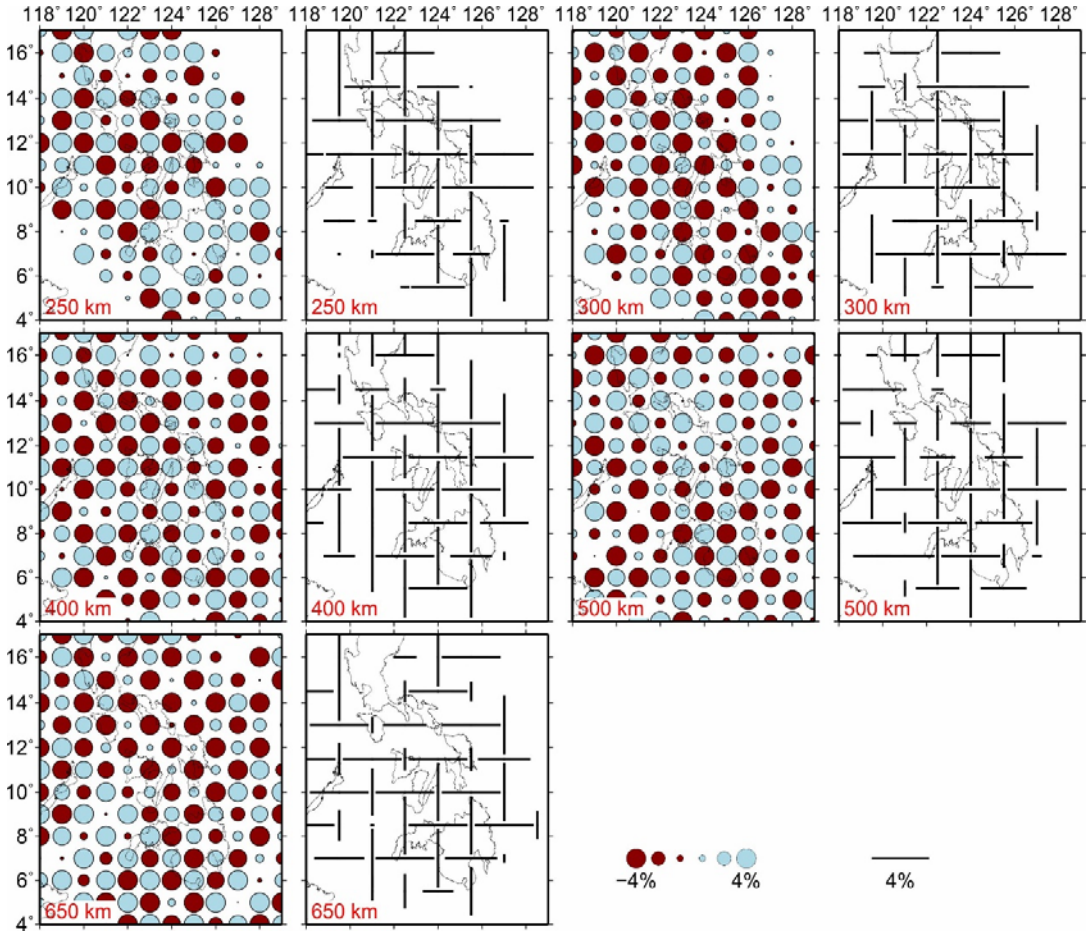

Fig. S24. (continued)

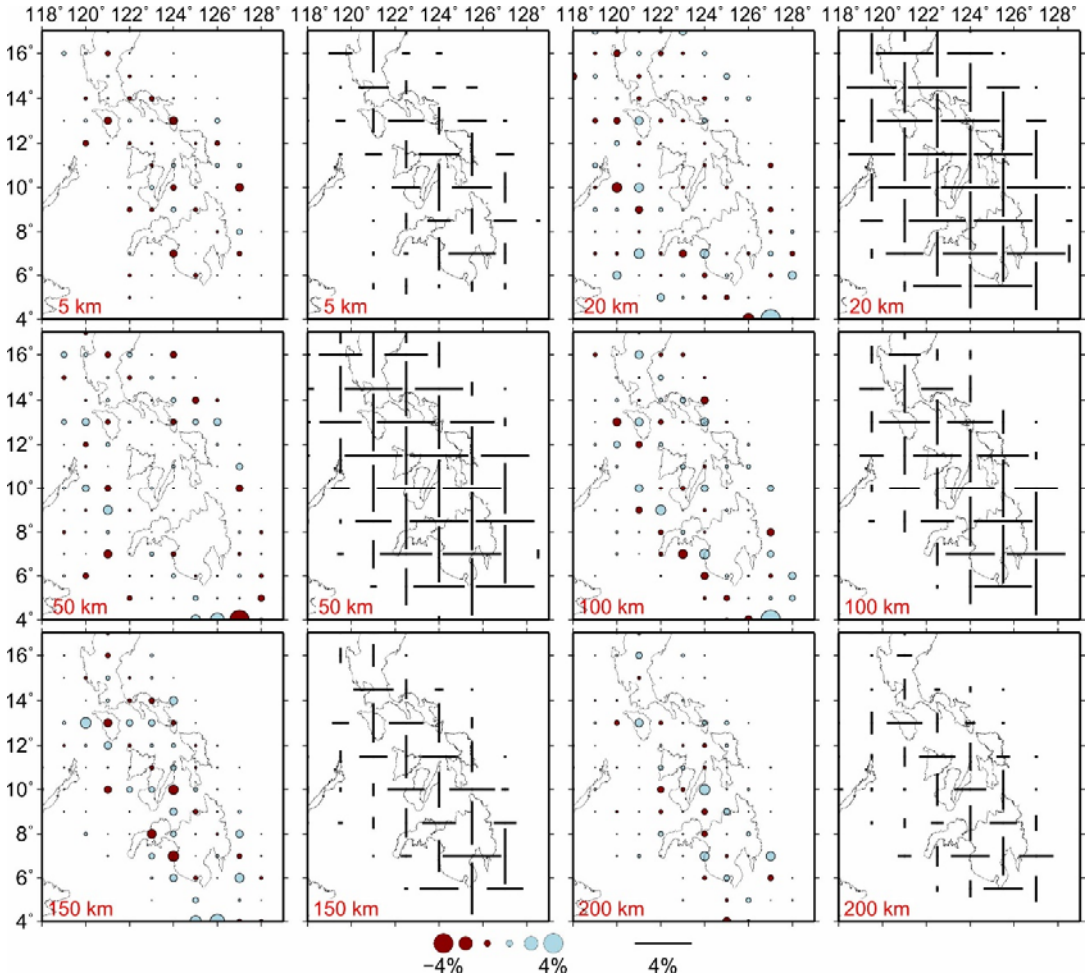

Fig. S25. The same as Fig. S24 but in the input model the radial anisotropic perturbations are ±4% and the isotropic Vp perturbation is 0**.**

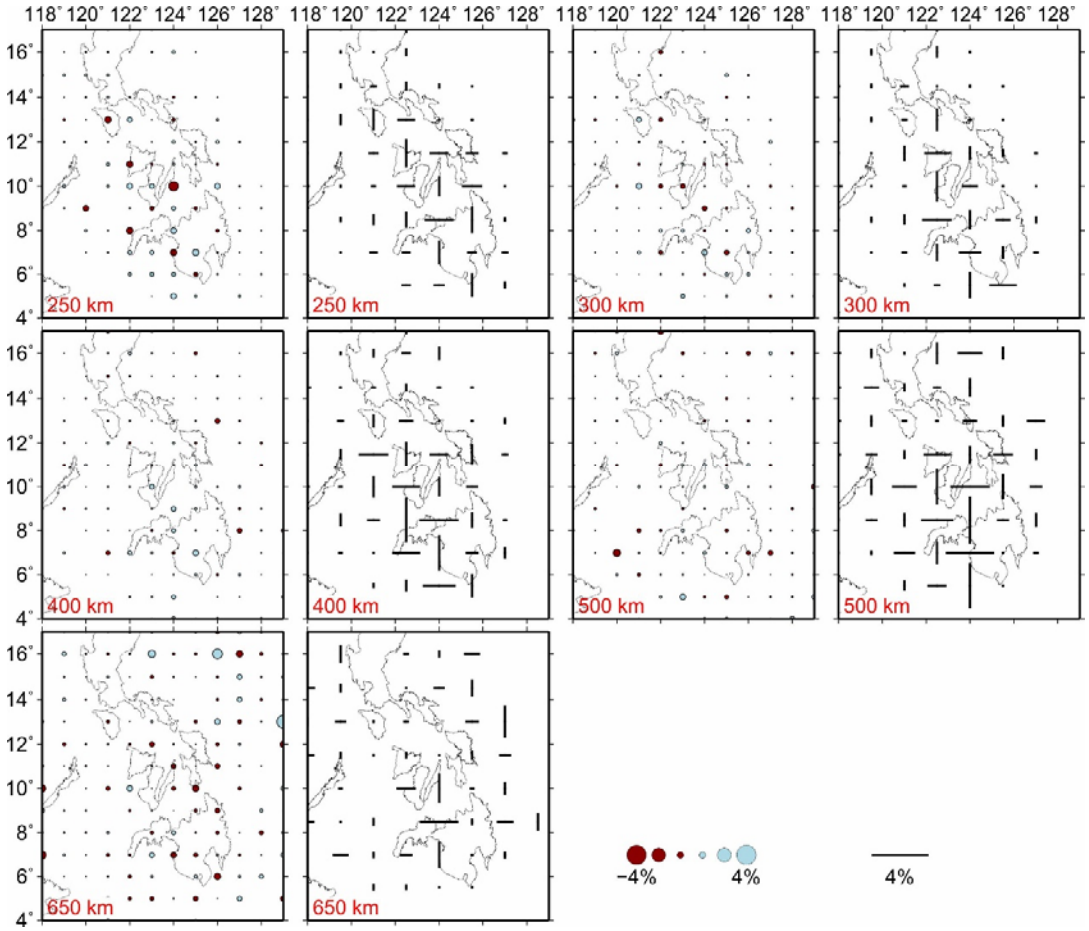

Fig. S25. (continued)

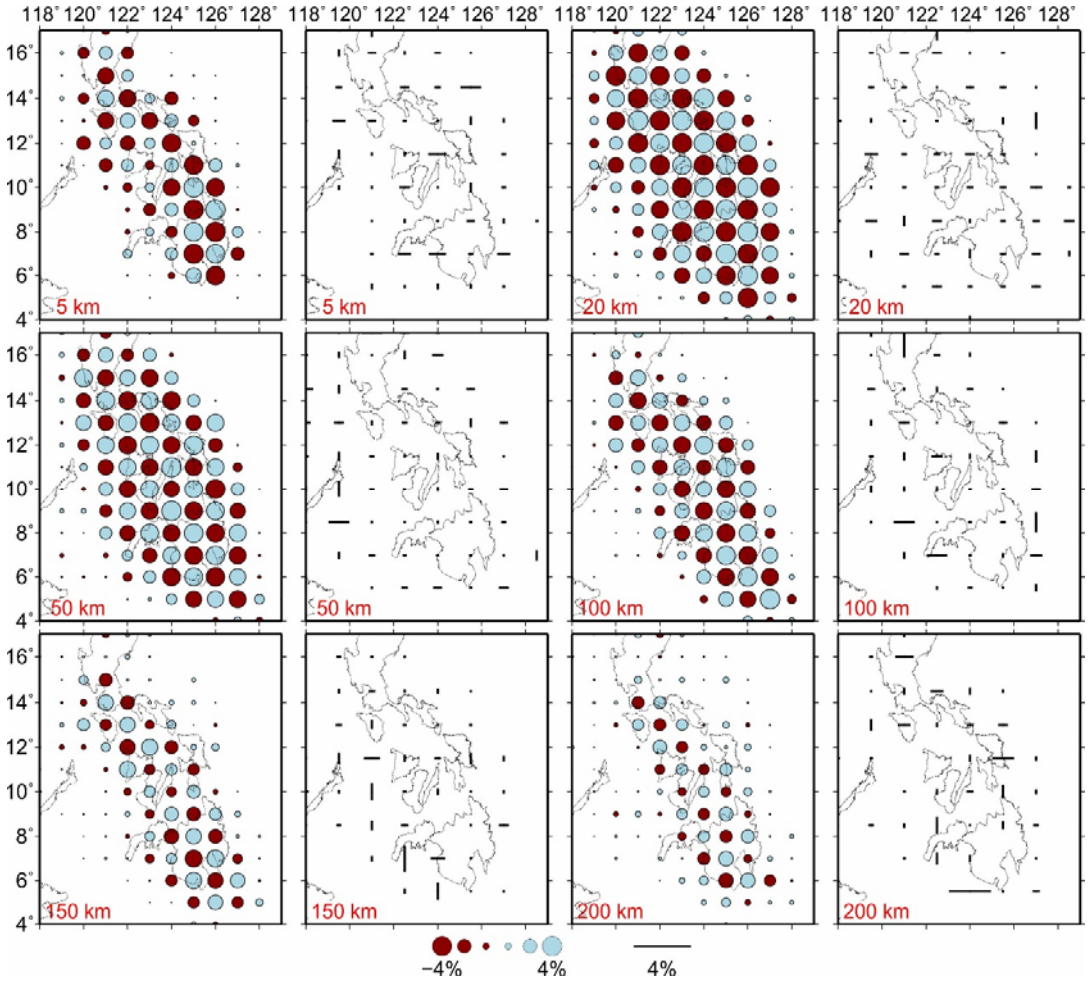

Fig. S26. The same as Fig. S24 but in the input model the isotropic Vp perturbations are ±4% and the radial anisotropic perturbation is 0.

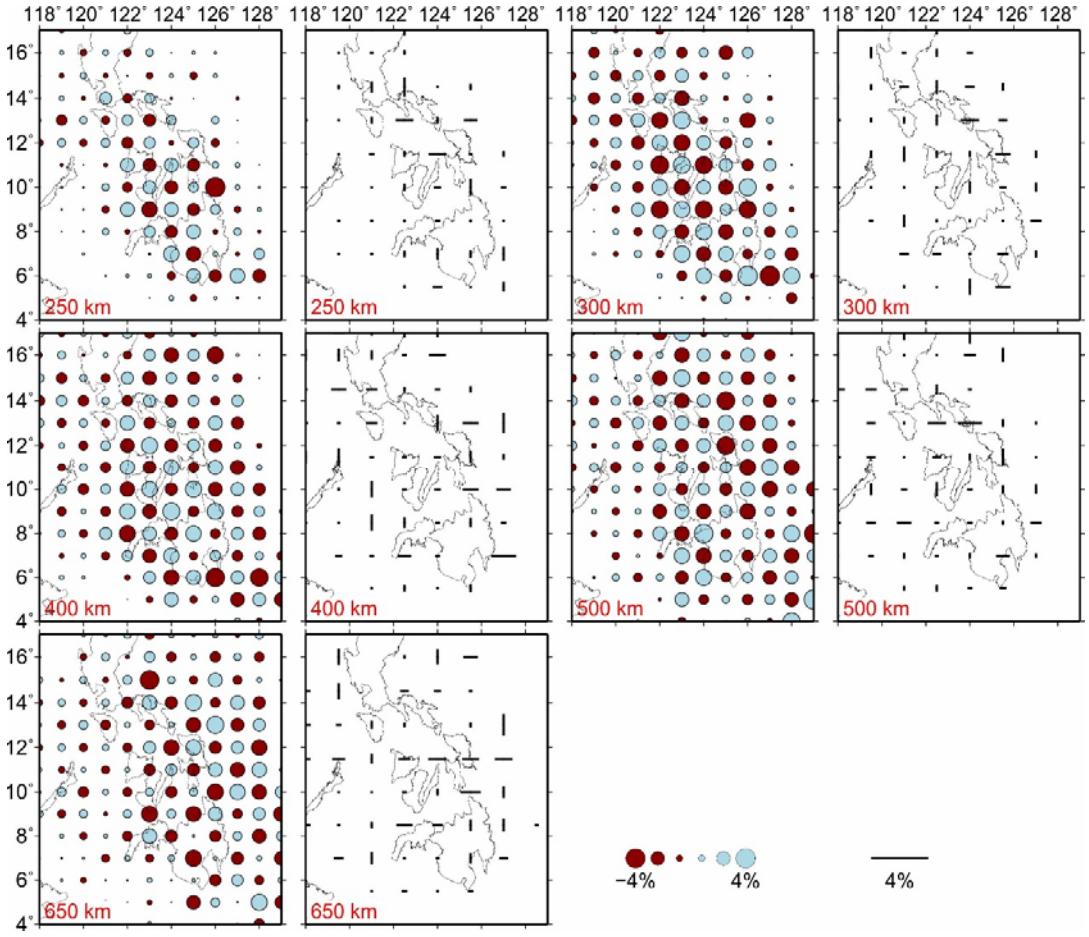

Fig. S26. (continued)

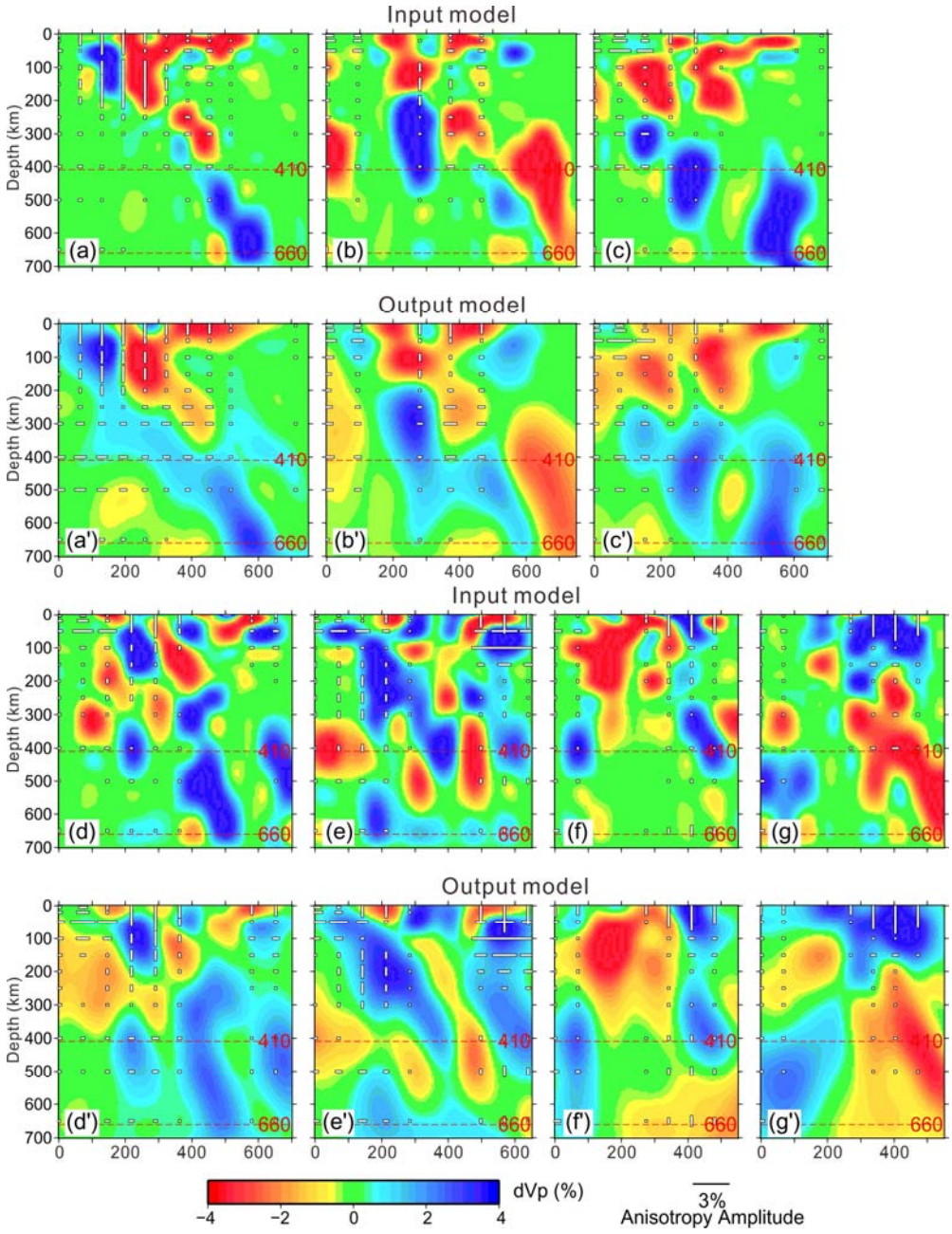

Fig. S27. Results of a RRT for P-wave radial anisotropy tomography. The obtained results (Fig. 6) are taken to be the input model, which are shown in the upper panels. Gaussian random noise with a standard deviation of 0.1 s is added to the theoretical travel times before the inversion. The red and blue colors denote low and high Vp perturbations, respectively. The horizontal and vertical bars represent the positive and negative radial anisotropies, respectively. The scales of the isotropic Vp and the radial anisotropy are shown at the bottom.

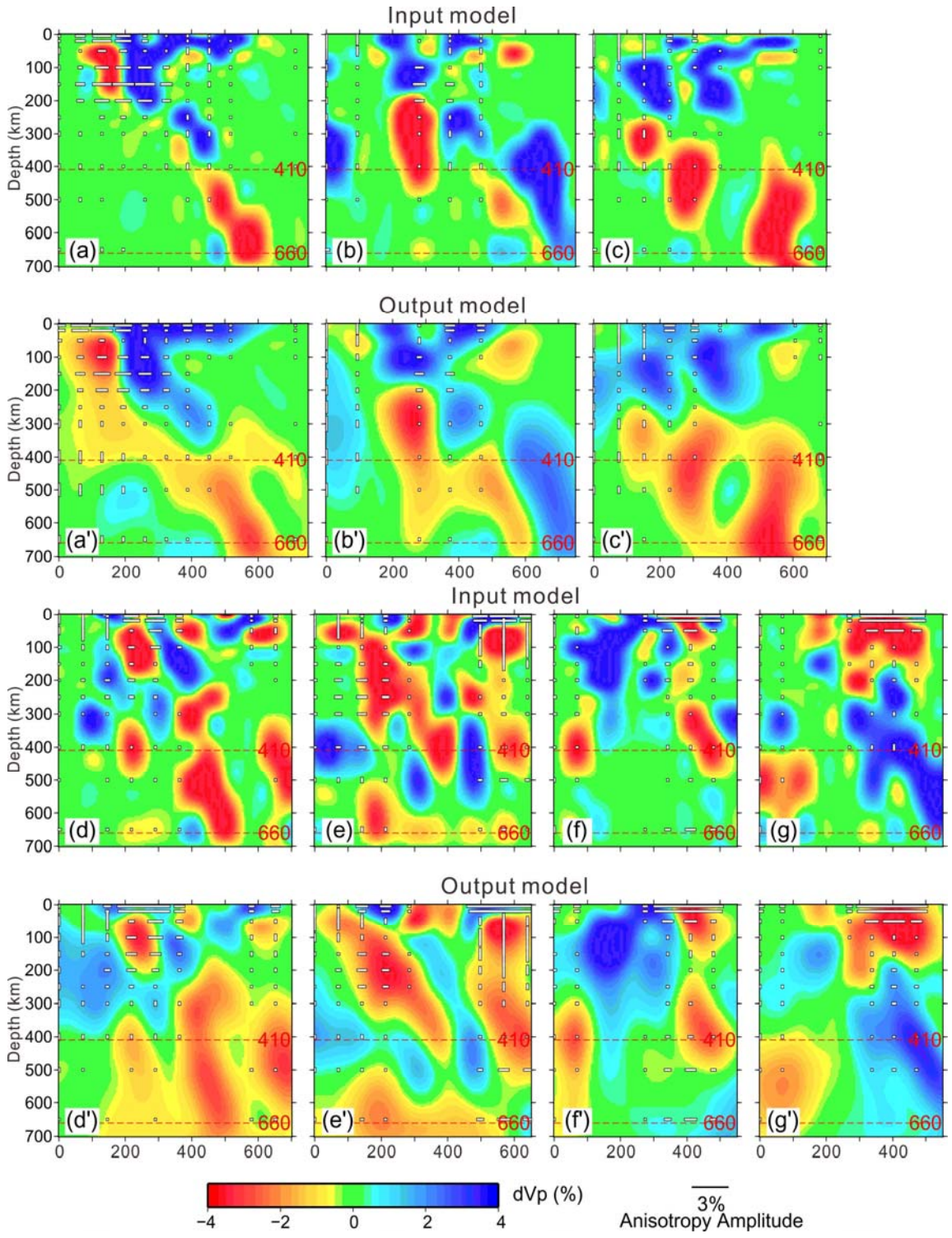

Fig. S28. The same as Fig. S27, but the patterns of the obtained radial anisotropy and the isotropic Vp (Fig. 6) are reversed and then taken to be the input model.

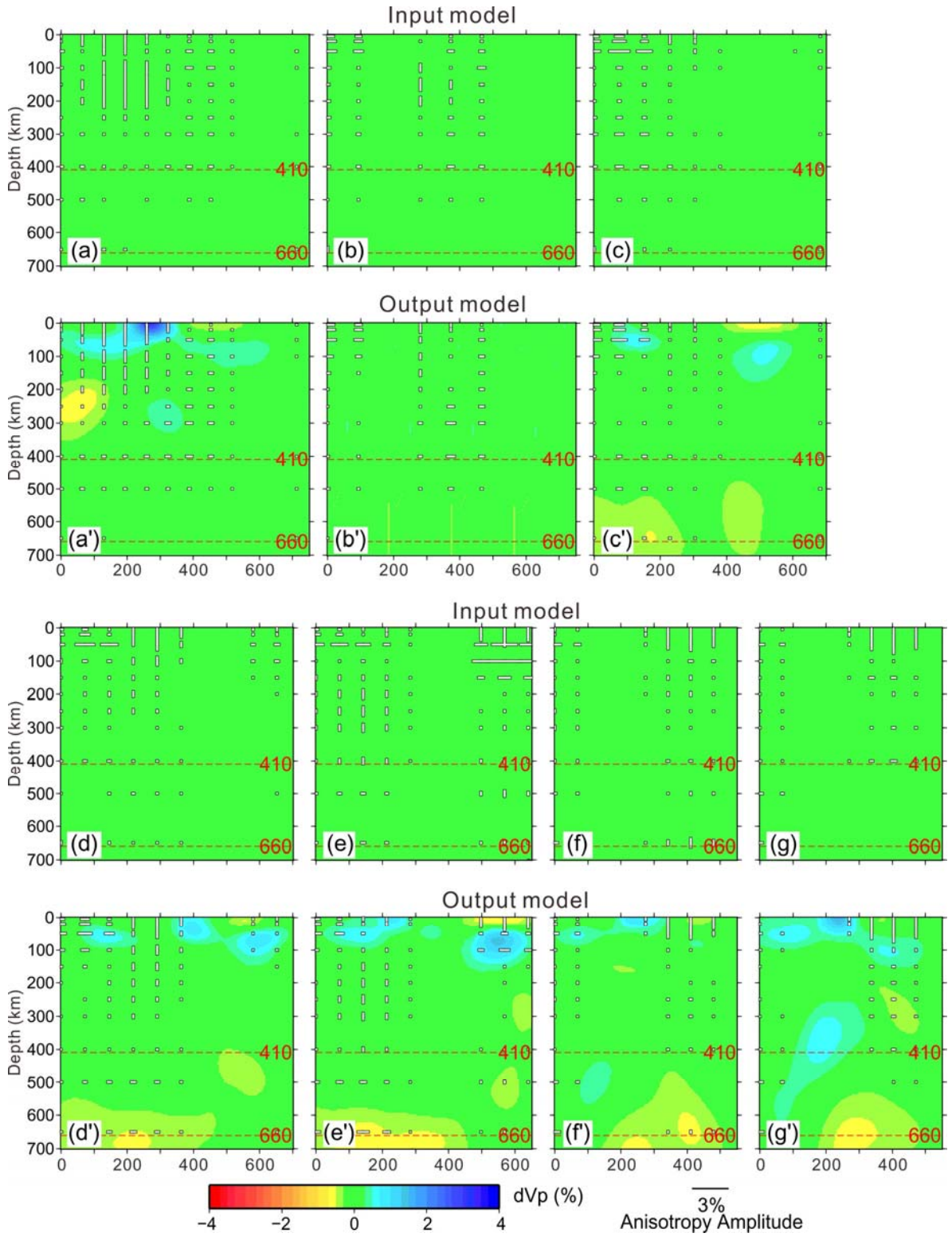

Fig. S29. The same as Fig. S27, but isotropic Vp anomalies are assumed to be zero in the input model.

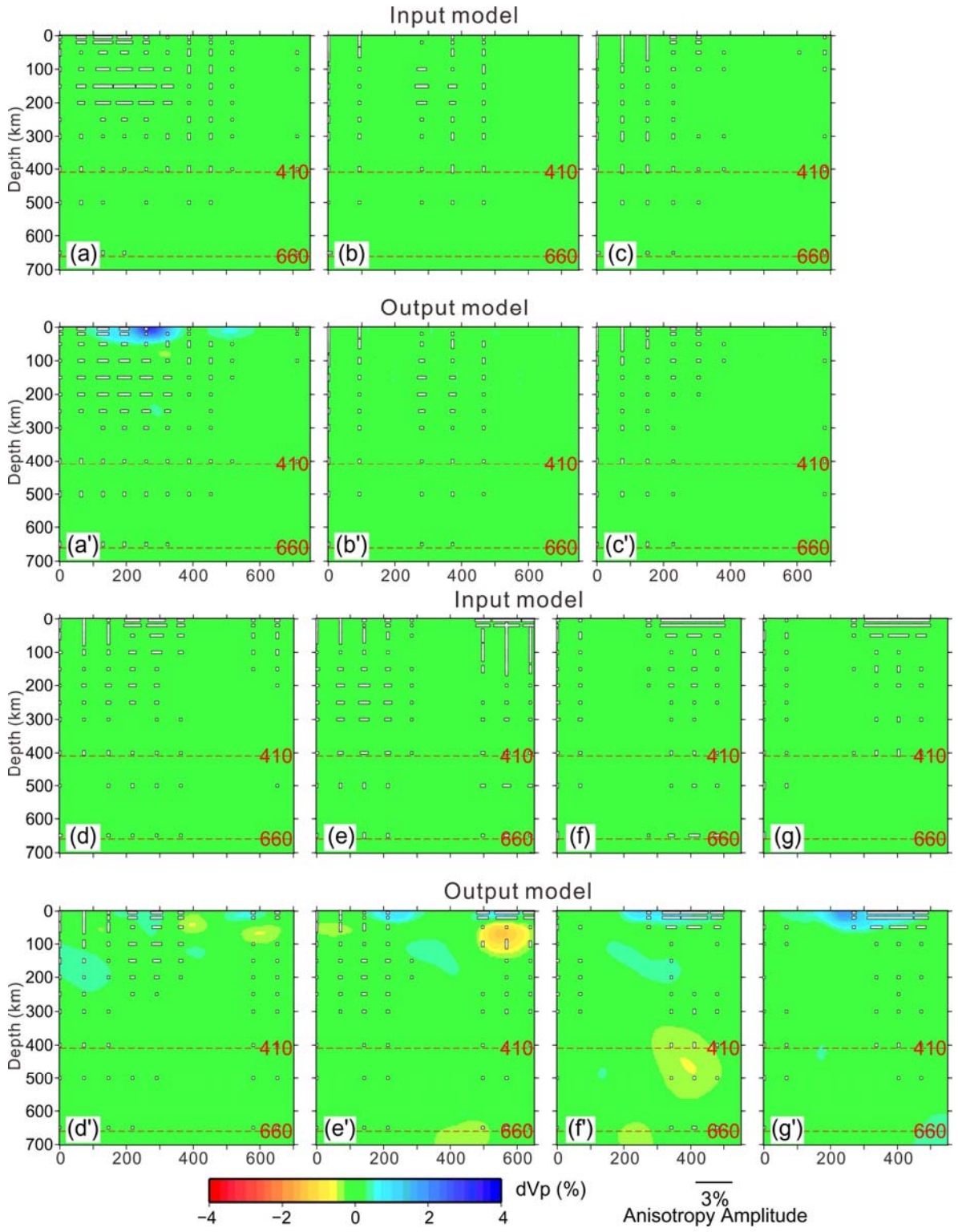

Fig. S30. The same as Fig. S27 but the pattern of radial anisotropy (Fig. 6) is reversed, and isotropic Vp perturbations are assumed to be zero in the input model.